

Behavior of passive polymeric tracers of different topologies in a dilute bath of active Brownian particles

Ramanand Singh Yadav ¹, Ralf Metzler ^{2,3,†} and Rajarshi Chakrabarti ^{1,*}

¹Department of Chemistry, Indian Institute of Technology Bombay, Mumbai 400076, India

²Institute of Physics and Astronomy, University of Potsdam, 14476 Potsdam, Germany

³Asia Pacific Centre for Theoretical Physics, Pohang 37673, Republic of Korea



(Received 26 August 2025; accepted 6 December 2025; published 20 January 2026)

Using computer simulations in two dimensions, we investigate the dynamics and structure of a passive polymeric tracer with different topologies immersed in a low-density active particle bath. One of the key observations is that polymers exhibit faster dynamics compared to passive colloidal particles at high activity, for the same particle density, in both linear and star polymer topologies. This enhanced motion is attributed to the accumulation of active particles, which induces prolonged and persistent movement of the polymer. Further analysis reveals that star polymers exhibit more complex and intriguing behavior than their linear counterparts. Notably, the accumulation of active particles promotes the pairing of arms in star polymers. For instance, a three-armed star polymer adopts a conformation similar to a linear polymer with two arms due to this pairing; as a result, at high activity, the dynamics of both the polymers converge. Finally, we explore the dynamics of a linear polymer with the same total number of beads as the star polymer. Interestingly, at high activity—where arm pairing in the star polymer is significant—the star polymer demonstrates faster dynamics than the linear polymer, despite having the identical number of beads. These findings contribute to a broader understanding of the interactions between active and passive components of varying topologies in dilute systems and highlight their potential for innovative applications ranging from materials science to biomedicine.

DOI: [10.1103/qrjy-9yt6](https://doi.org/10.1103/qrjy-9yt6)

I. INTRODUCTION

Active matter is constituted of small units that convert their internal energy—typically replenished periodically from their environment—into directed motion. Unlike passive systems, active matter exhibits nonthermal fluctuations, breaks detailed balance, and violates the fluctuation-dissipation relation, keeping the system inherently out of equilibrium [1,2]. These characteristics enable intriguing behaviors and potential applications, such as targeted cargo transport and efficient delivery in both biological (*in vivo*) and laboratory (*in vitro*) environments. Several studies have been dedicated to understanding how active forces interact with thermodynamic forces [1,3–9], and to exploring ways to harness these forces for specific microscale tasks [10,11].

The coexistence of active and passive elements is a key feature of many living systems. For instance, the motility of microorganisms in active systems plays a crucial role in nutrient mixing and maintaining ecological balance in aquatic environments [12,13]. The enhanced diffusion of passive

components in an active bath affects various passive entities such as enzymes, granules, and extracellular products [14]. These components are influenced by cyclic conformational changes in biomolecules such as DNA and RNA during active transcription processes, which are fueled by ATP [15].

Recent studies have explored the statistical mechanics of active agents in a passive bath [16–18] as well as passive agents in an active bath [19–34]. In contrast to spherical passive colloidal particles in an active bath, asymmetric passive agents—such as V-shaped wedges—exhibit a more pronounced directed motion. This occurs because active particles tend to accumulate in the cusp of the wedge, exerting an asymmetric pressure on its walls and driving a persistent movement [35,36]. In a passive bath, in contrast, the pressure exerted by passive particles is isotropic, resulting in no net directional motion.

The simple model system of a passive tracer in an active bath has been explored both numerically and experimentally by various groups [35–37]. It has been observed that maximal efficiency occurs at an optimal number of active particles. At high packing fractions, the bath becomes jammed, which restricts the mobility of the carrier object [38]. Conversely, at low packing fractions, there is insufficient accumulation of active particles near the object to induce significant motion. Unlike hard asymmetric objects, soft and flexible objects in an active bath display intriguing behaviors. Several studies have investigated the interactions between active particles and deformable passive objects, as well as the behavior of active polymers [39,40]. A linear polymer immersed in a bath of

*Contact author: rajarshi@chem.iitb.ac.in

†Contact author: rmetzler@uni-potsdam.de

Published by the American Physical Society under the terms of the Creative Commons Attribution 4.0 International license. Further distribution of this work must maintain attribution to the author(s) and the published article's title, journal citation, and DOI.

active Brownian particles (ABPs) adopts different conformations depending on its stiffness. For instance, a semiflexible linear polymer forms transient hairpin structures due to the accumulation of ABPs in regions of high curvature, which promotes polymer shrinkage. In contrast, a fully flexible polymer tends to expand with increasing activity [22,28,30]. Similar to hard passive asymmetric objects, flexible linear polymers also exhibit enhanced dynamics, driven by the localized accumulation of active particles in highly curved (“parachute-shaped”) regions [28]. While previous studies have focused on linear polymer topologies, less attention has been given to branched and star-shaped polymers in active baths. Star-shaped polymers, in which multiple arms are connected at a central core, have biological counterparts in the form of certain viruses, such as astroviruses [41]. Some studies have also engineered star-shaped molecules to mimic viral properties, investigating their dynamics [42,43]. Moreover, the tunable properties of star-shaped polymers have made them an attractive candidate for drug delivery applications [44–48]. While computational studies have examined the behavior of star polymers in passive baths (both good and bad solvents) [49], investigating their conformational changes and dynamics, there is still limited research on the behavior of star-shaped polymers in an active bath [38].

In this work, we explore the dynamics and conformational changes of star polymers and compare their behavior to that of tracers with other topologies in a dilute bath of ABPs using computer simulations in two dimensions. We observe an intriguing conformational behavior of the star-shaped polymers in such an environment. Notably, beyond a threshold value of the active force, a “folded” conformation emerges for the star polymer with three arms, such that two arms are paired while the third remains at a distance. This occurs due to the asymmetric accumulation of active particles. In previous studies, a similar behavior has also been observed in systems of flexible polymers, where increased activity at low packing fractions promotes the pairing of two polymer chains [50]. In contrast, at relatively high densities, active particles can form dynamic crystalline structures, establishing a stable, oscillating bridge between particles. This bridge gives rise to significant long-range dynamic repulsion during wetting near confining boundaries. However, as the density decreases, the bridge gradually breaks down, resulting in an intriguing transition to long-range dynamic depletion attraction [38,51,52]. The pairing of the arms, together with the accumulation of active particles, drives prolonged directed motion. This is evident from the increased mean-squared displacement (MSD), the positive temporal velocity autocorrelation function (VACF), and the enhanced persistence time with increasing activity.

The described arm pairing in star polymers is more favorable and occurs at lower activity levels for semiflexible polymers as compared to flexible ones. When comparing the behavior of a star polymer with that of passive colloidal particles—whose size is similar to that of a single bead of the polymer—we find that the dynamics of the star polymer’s center of mass is faster and more persistent at high activity. This is attributed to the accumulation of active particles and the pairing of arms. The difference is evident in the higher MSD of the star polymer’s center of mass compared to that of the colloidal particle at long times and high activity.

Additionally, the star polymer exhibits a larger scaling exponent of the MSD and a more pronounced positive temporal VACF under these conditions. Interestingly, at high activity the conformation of the star polymer—in which two arms are paired and the third is extended—resembles that of a linear polymer. To gain a clearer understanding, we compare the behavior of a three-armed star polymer (with 61 beads) with that of a linear polymer (41 beads), and our findings suggest that their dynamics converge at high activity. Additionally, we compare the star polymer with a linear polymer containing the same number of beads. The results indicate that, at high activity—where arm pairing in the star polymer is significant—the dynamics of the star polymer are slightly faster and more persistent than those of the linear polymer, despite having the same number of beads. This difference can be explained by the distribution of the radius of gyration, as the linear polymer exhibits a significantly larger radius of gyration compared to the star polymer. Additionally, the time evolution of the VACF shows that the star polymer maintains a higher correlation as compared to the linear polymer. In the present study, the size of the aABPs is taken to be equal to the bead size of the passive polymer. Previous studies have explored the effect of relative size differences between active particles and crowders, showing that larger crowders lead to stronger accumulation of active particles [53–55]. In the context of our study—examining star polymers in an active bath—when the polymer beads are relatively larger than the ABPs, we expect a more pronounced accumulation of ABPs around the polymer. However, increasing the bead size also reduces the dynamics of the polymer’s center of mass. A systematic investigation of this size effect would indeed be interesting and is planned for future work. This paper is organized as follows. In Sec. II, we present the model and simulation details. Results and discussion are presented in Sec. III and finally, we conclude the paper in Sec. IV. Additional information is compiled in the Appendix.

II. MODEL AND SIMULATION DETAILS

We carry out coarse-grained computer simulations of a passive tracer embedded in a low-density dry active bath of ABPs, in two dimensions with periodic boundary conditions. The considered tracers include passive colloidal particles, linear polymers with 41 and 61 monomers, and the star polymer with three ($N_{\text{arm}} = 3$) and four arms ($N_{\text{arm}} = 4$), in which each arm consists of 20 monomers and is connected with a central monomer. The diameter of the individual tracer particles and the monomers of the polymeric objects is σ , the same size as the bath ABPs. To set up the system, we fix the passive tracer in a square box of length 120σ populated with ABPs. A schematic of our system is shown in Fig. 1. In the simulations, we consider packing fractions of the bath $\phi = 0.06$ and $\phi = 0.15$, where ϕ is defined as $\phi = \frac{N_{\text{ABP}}A_{\text{ABP}}}{120\sigma \times 120\sigma}$. Here, $A_{\text{ABP}} = \pi(\frac{\sigma}{2})^2$ is the area of a single ABP.

The dynamics of the position $\mathbf{r}_i(t)$ of the i th particle of mass m is described by the Langevin equation

$$m \frac{d^2 \mathbf{r}_i(t)}{dt^2} = -\gamma \frac{d\mathbf{r}_i}{dt} - \sum_j \nabla V(\mathbf{r}_i - \mathbf{r}_j) + \mathbf{f}_i(t) + F \mathbf{e}(\theta_i). \quad (1)$$

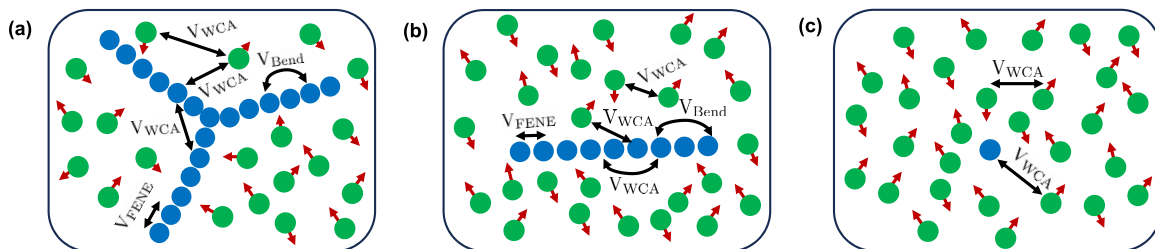


FIG. 1. Schematic of the model system (not to scale): (a) a single star polymer with three arms (blue). (b) A passive linear polymer (blue). (c) A single passive particle (blue). Each of these systems is simulated separately while immersed in a dilute bath of ABPs (green). The red arrows indicate the instantaneous directions of the ABPs. Pairwise nonbonded interactions among the polymer beads, between the polymer beads and ABPs, between passive particles and ABPs, and among the ABPs themselves are modeled using the WCA potential, represented by double-headed arrows. Additionally, the neighboring beads of the polymer are connected via the FENE potential, and a bending potential is applied to restrict polymer bending.

In the overdamped limit, the inertial term $m \frac{d^2 \mathbf{r}_i(t)}{dt^2}$ is negligibly small as compared to the drag force $\gamma \frac{d\mathbf{r}_i}{dt}$, where γ is the friction coefficient. To ensure that the system is practically overdamped, we took the comparatively high value of $\gamma = 200$. For this choice, the momentum relaxation time, $\tau_{\text{rel}} = m/\gamma$, remains quite short—about 5×10^{-3} (in units of the elementary time $\tau_0 = \sqrt{m\sigma^2/\epsilon}$, where σ , ϵ , and m are the fundamental Lennard-Jones units of length, energy, and mass, respectively). In contrast, the characteristic Brownian dynamics timescale—the time it takes a particle to diffuse a distance comparable to its own size—is given by $\tau_{\text{BD}} \sim \frac{\gamma\sigma^2}{k_B T} = 200$ (in units of τ_0). For this high friction coefficient, we have $\frac{m}{\gamma} = 5 \times 10^{-3} \tau \ll \frac{\gamma\sigma^2}{k_B T} = 200\tau$, which ensures that inertial effects are negligible and the system operates in the Brownian (overdamped) regime. This approach has been widely adopted in the literature [28,40,56]. The k th component $f_{ik}(t)$ of the thermal force \mathbf{f}_i on particle i is taken as an independent Gaussian white noise with zero mean and variance $\langle f_{ik}(t)f_{jl}(t') \rangle = 2\gamma k_B T \delta_{ij} \delta_{kl} \delta(t-t')$, where δ_{ij} is the Kronecker delta and $\delta(t)$ is the Dirac δ function. Moreover, $k_B T$ represents the thermal energy in terms of the Boltzmann constant k_B and the absolute temperature T . The ABPs are simulated as disks of diameter σ moving under the action of a constant force F along a predefined orientation vector $\mathbf{e}(\theta_i) = \{\cos(\theta_i), \sin(\theta_i)\}$. $F\mathbf{e}$ is thus the active force (“propulsion strength”) of magnitude F of the ABPs that drives the system out of equilibrium. The dimensionless Péclet number can be used to express this propulsion strength relative to the thermal particle speed as $\text{Pe} = \frac{v\sigma}{D} = \frac{F\sigma}{k_B T}$ such that $\text{Pe} = 0$ for passive tracers and $\text{Pe} > 0$ for the ABPs.

The orientation θ_i of the velocity of the i th ABP is a function of time according to the stochastic equation

$$\frac{d\theta_i}{dt} = \sqrt{2D_R} \boldsymbol{\eta}(t). \quad (2)$$

Here, D_R is the rotational diffusion coefficient, which is related to the persistence time τ_R of an ABP by the relation $\tau_R = 1/D_R$ [57]. The term $\boldsymbol{\eta}(t)$ represents a zero-mean Gaussian random vector with unit variance. We again assume componentwise and particle-particle independence, i.e., $\langle \eta_{ik}(t)\eta_{jl}(t') \rangle = 2D_R \delta_{ki} \delta_{lj} \delta(t-t')$, where $\eta_{ik}(t)$ is the k th component of the noise acting on particle i .

The total pairwise interaction potential $V(r_i - r_j)$ is defined as $V = V_{\text{WCA}} + V_{\text{FENE}} + V_{\text{Bend}}$. Here, the monomers of the polymers are connected by the finitely extensible nonlinear elastic (FENE) potential

$$V_{\text{FENE}}(r_{ij}) = \begin{cases} -\frac{Kr_{\text{max}}^2}{2} \log \left(1 - \left[\frac{r_{ij}}{r_{\text{max}}} \right]^2 \right), & r_{ij} \leq r_{\text{max}}, \\ = \infty, & \text{otherwise,} \end{cases} \quad (3)$$

where $r_{ij} = |\mathbf{r}_i - \mathbf{r}_j|$ represents the separation between monomers i and j (with position vectors \mathbf{r}_i and \mathbf{r}_j , respectively) of the polymer; $r_{\text{max}} = 1.5\sigma$ is taken as the upper limit of r_{ij} and K denotes the force constant, which accounts for the stiffness of the polymer. To restrict the bending of the polymer, we introduce the bending potential

$$V_{\text{Bend}} = \kappa (1 - \cos(\phi_{\text{bend}})), \quad (4)$$

where $\kappa = 75$ (in units of $k_B T$) lies in the range in which the polymer behaves as a stiff, semiflexible chain [58], and ϕ_{bend} denotes the angle between two successive bond vectors of the polymer. We employ purely repulsive pairwise nonbonded interactions between the monomers of the polymers, modeled in terms of the Weeks-Chandler-Andersen (WCA) potential [59]

$$V_{\text{WCA}}(r_{ij}) = \begin{cases} 4\epsilon_{ij} \left(\left[\frac{\sigma_{ij}}{r_{ij}} \right]^{12} - \left[\frac{\sigma_{ij}}{r_{ij}} \right]^6 \right) + \epsilon_{ij}, & \text{if } r_{ij} \leq 2^{1/6} \sigma_{ij}, \\ = 0, & \text{otherwise.} \end{cases} \quad (5)$$

Here, ϵ_{ij} is the strength of the interaction with the effective interaction diameter $\sigma_{ij} = (\sigma_i + \sigma_j)/2$.

All simulations are performed using a Langevin thermostat, and the equation of motion is integrated using the velocity Verlet algorithm in each time step [60]. We initialize the system by placing the passive tracer in the center of the bath and relaxing the initial configuration for 10^7 steps. The simulations are carried out for 6×10^8 steps, where the integration time step is taken to be 5×10^{-4} , and the positions of the monomers are recorded every 100th step. The simulations are carried out using LAMMPS [61], a freely available open-source molecular dynamics package. In our simulations, we measure the length in units of σ and the energy in units of thermal energy $\epsilon = k_B T$. All other physical quantities are therefore presented in dimensionless units expressed in terms

TABLE I. Model parameters used in our simulations.

Parameter	Value
σ_{ABP}	σ
σ_{beads}	σ
N_{ABP}	1101 ($\phi = 0.06$) and 2751 ($\phi = 0.15$)
$\frac{m}{\gamma}$	5×10^{-3}
$k_B T$	1
Δt	5×10^{-4}
Pe	0, 5, 10, 15, and 20 30, 40, 50, and 60

of these fundamental units σ , ϵ , and m . Details of the model parameters are given in Table I.

III. RESULTS AND DISCUSSION

A. Behavior of a three-armed star polymer in a dilute active bath

Soft particles represent a class of materials with a “dual nature,” in the sense that they exhibit properties that fall in between those of hard colloids and polymer coils [62]. Typical examples include microgels [63], micelles [64], and star polymers [64,65], whose phase behavior and dynamics are strongly influenced by their degree of softness. In this context, multiarm star-shaped systems—with adjustable arm

number, length, and flexibility—offer a versatile platform for investigating how varying degrees of “softness” influence the dynamic behavior, due to their tunable deformability and potential for interdigitation. In literature, it was studied how the softness of a material can be modulated by the doping with active particles [66], and can influence the conformation and dynamics of the polymer, which has been extensively studied for linear polymers [28,39,40]. Here, in this work, we explore the behavior of a three-armed star polymer in a dilute bath of active particles, specifically, the dynamics, and the conformational changes and observe some intriguing behavior.

1. Conformational changes of the star polymer

In contrast to linear polymers, star polymers exhibit a more intricate architecture due to their multiple arms [64,65,67–69]. To characterize their structural features, we compute the pairwise center-of-mass separation

$$R_{A_i-A_j} = \sqrt{(x_{\text{com}(i)} - x_{\text{com}(j)})^2 + (y_{\text{com}(i)} - y_{\text{com}(j)})^2} \quad (6)$$

for $i, j = 1, 2, 3$ between the three arms of a three-armed flexible ($\kappa = 0$) star polymer.

Figure 2(a) presents the probability density of this separation $R_{A_i-A_j}$ for all possible combinations of i and j ($i, j = 1, 2, 3$), for varying Péclet number Pe of the surrounding active bath particles. As Pe increases (we vary it in the range $\text{Pe} = 0, \dots, 30$), the distribution initially broadens,

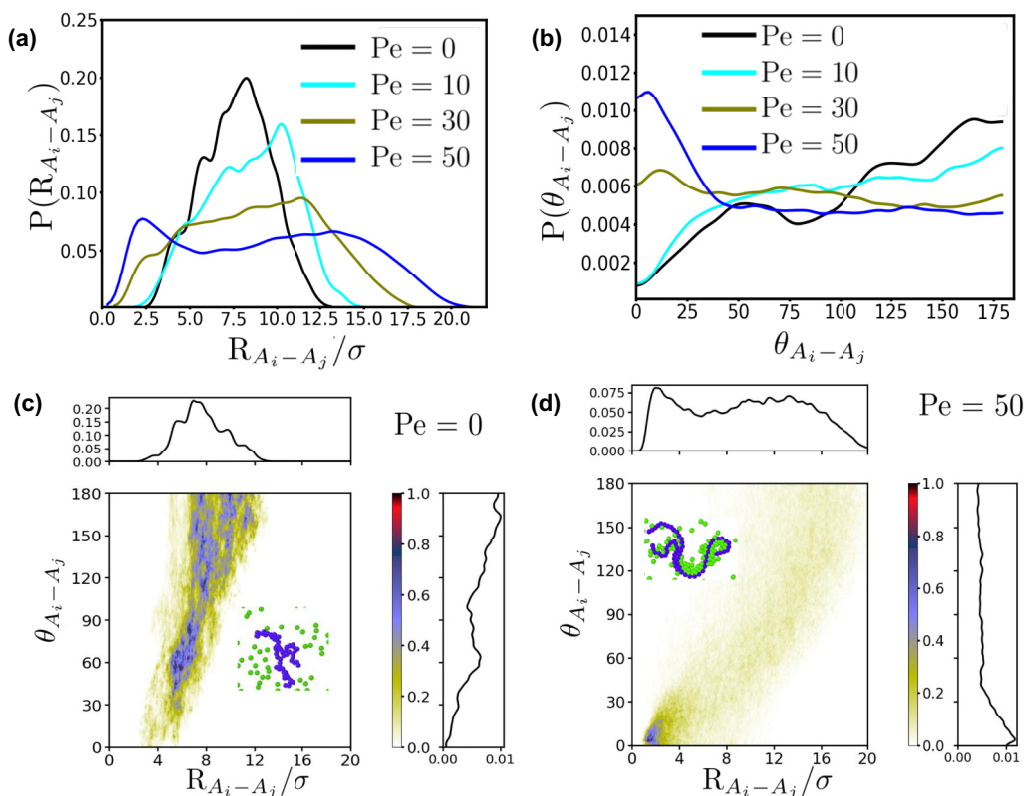


FIG. 2. Probability density functions of (a) the arm-arm separation $R_{A_i-A_j}$ and (b) the arm-arm angle $\theta_{A_i-A_j}$ for different values of the Péclet number Pe. Panels (c) and (d) show the 1D and 2D probability of $R_{A_i-A_j}$ and $\theta_{A_i-A_j}$ for Pe = 0 and Pe = 50, respectively. Snapshots of conformations of the star polymer and associated ABPs shown in panels (c) and (d) demonstrate the accumulation of ABPs induced by higher activity.

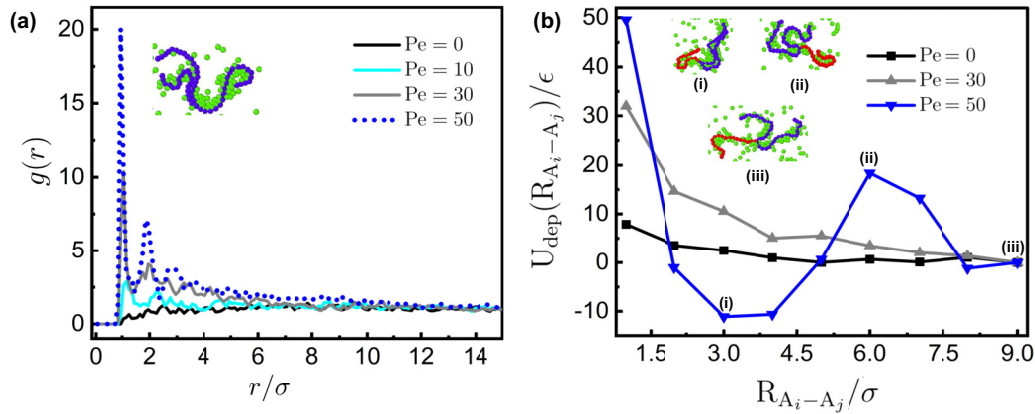


FIG. 3. Radial distribution function $g(r)$ of ABPs surrounding (a) a star polymer for different Pe . The inset in panel (a) shows a snapshot of the system with the star polymer immersed in an active bath at $Pe = 50$. (b) Effective interaction potential between a pair of arms (blue) of the star polymer as a function of their separation $R_{A_i-A_j}$ for different values of Pe . The insets in panel (b) show the conformations of the star polymer for a given separation $R_{A_i-A_j}$: (i) 3.0, (ii) 6.0, and (iii) 9.0.

indicating enhanced fluctuations in the arm separations as shown in Movie_S1 and Movie_S2 (see Appendix H and Supplemental Material [70]). At high activity ($Pe = 50$), a pronounced peak appears at smaller values of $R_{A_i-A_j}$, followed by a broad distribution of the population at larger separations. The peak at lower $R_{A_i-A_j}$ does not occur exactly at $R_{A_i-A_j}/\sigma = 1.0$, due to the self-avoidance of the polymer beads and the accumulation of some ABPs between the arms [50]. The bimodality of the distribution is characteristic of a transient pairing of two arms, while the third remains spatially separated, fluctuating over time as shown in Movie_S3 (see Appendix H and Supplemental Material [70]). To gain further insight into this pairing behavior, we calculate the angle $\theta_{A_i-A_j}$,

$$\theta_{A_i-A_j} = \cos^{-1} \left(\frac{\mathbf{A}_i \cdot \mathbf{A}_j}{|\mathbf{A}_i||\mathbf{A}_j|} \right) \quad (7)$$

between the arm vectors, where $\mathbf{A}_i = (x_i^{\text{term}} - x_i^c, y_i^{\text{term}} - y_i^c)$, and \mathbf{A}_j is defined analogously. Here, the superscript “c” refers to the central bead of the star polymer, and “term” denotes the terminal beads of the polymer.

As shown in Fig. 2(b), the distribution of the arm-arm angle $\theta_{A_i-A_j}$ develops a sharp peak at lower angles with increasing Pe , particularly between $Pe = 30$ and $Pe = 50$. This indicates the emergence of a preferential alignment or pairing between two arms. A broader component at larger angles persists, reflecting the variability in the orientation of the third arm.

Figs. 2(c) and 2(d) display the joint probability density of $R_{A_i-A_j}$ and $\theta_{A_i-A_j}$ at $Pe = 0$ and $Pe = 50$, respectively. At equilibrium ($Pe = 0$), the distribution is centered around moderate values of $(R_{A_i-A_j})$ with a broad angular spread, consistent with a disordered, coil-like conformation. In contrast, under strong activity conditions ($Pe = 50$), the distribution becomes varied, with a significant population concentrated at low values of both $R_{A_i-A_j}$ and $\theta_{A_i-A_j}$, indicative of a paired-arm configuration. A secondary population at higher values of both parameters corresponds to the fluctuating, unpaired third arm. These results suggest that at high activity, the star polymer indeed adopts a dynamic-induced asymmetric

conformation wherein two arms transiently associate, effectively forming a linear structure with the third arm extending outward.

The accumulation of active particles near a polymer has a significant effect on the conformation it adopts in the active bath. For instance, conformations such as the bent structure of a semiflexible linear polymer or the looping of an end-attractive linear polymer are strongly influenced by the presence of active particles [28,38,71]. To understand the behavior of a star polymer, with its much complex structure as compared to its linear counterpart, in an active bath, we calculate the radial distribution function $g(r)$, of ABPs around the polymer, as shown in Fig. 3(a). We observe a noticeable accumulation of ABPs in the vicinity of the chain. This accumulation becomes more pronounced with increasing Pe , reflected in the increasing height of the peak of $g(r)$ at $r = 1$. We also observe that with the bath increasing activity, not only does the peak at $r = 1$ become more pronounced, but also a secondary peak emerges at a larger distance. The inset in Fig. 3(a) shows a snapshot detailing that ABP accumulation predominantly occurs in regions of higher curvature. This suggests that both the accumulation and the resulting bent conformation of the polymer are more favorable at higher Pe . Another interesting observation is the pairing of the arms of the star polymer at high activity, enabling it to adopt a conformation similar to that of a linear polymer.

At high activity, the accumulation of active particles facilitates the formation of an asymmetric polymer structure—specifically, the pairing of two arms while the third arm remains separate. To understand the relationship between the adopted conformation and ABP accumulation, we calculated the effective interaction energy between two arms of the star polymer (details provided in Appendix A), relative to the conformation with $R_{A_i-A_j} = 9.0$, the value corresponding to their separation at $Pe = 0$, as a function of $R_{A_i-A_j}$ for various values of Pe . To perform this calculation, a biased potential was applied between the two arms [shown in blue in the snapshot of Fig. 3(b)] to achieve a particular separation. In this setup, the accumulation of active particles near the

selected arms and their separation serve as defining parameters for the energy. In Fig. 3(b), in the absence of activity with $Pe = 0$, the energy profile remains nearly flat around zero, except for a positive deviation at around $R_{A_i-A_j} = 1.0$, which arises due to the self-avoidance of the polymer beads. At finite activity with $Pe = 30$, the energy profile indicates that conformations with smaller separations around $R_{A_i-A_j} = 1.0$ are less stable than those with larger separations. Interestingly, at relatively high activity with $Pe = 50$, the energy profile shows a stabilization of conformations with a smaller distance around $R_{A_i-A_j} \approx 3$, supporting the tendency of the arms to pair at high activity. This stabilization of conformations, such that the separation between arms is minimized, goes hand in hand with the significant accumulation of ABPs at such high activity levels. Therefore, we conclude that the stabilization of paired-arm conformations is facilitated by the asymmetric accumulation and the resulting exerted pressure of active particles on the polymer arms. Such effective attractions between passive tracers in an active bath have been previously reported. For example, when two passive particles are immersed in a bacterial bath, a short-range “attraction” emerges between them as the level of activity in the bath increases [52]. Similar short-range attractions have also been observed for a linear polymer chain and a rigid rod in a bath of ABPs [50,51]. In all cases shown in Fig. 3(b), the depletion potential $U_{\text{dep}}(R_{A_i-A_j})$ shows a significant positive value at $R_{A_i-A_j} = 1.0$, which increases with growing Pe . This confirms that the high positive value of $U_{\text{dep}}(R_{A_i-A_j})$ at short distances arises due to both polymer self-avoidance and the limited presence of ABPs between the arms, a direct consequence of the star polymer geometry.

The inclusion of rigidity in a polymer exhibits more interesting features in an active bath. For instance, a semiflexible linear polymer ($\kappa > 0$) adopts a hairpinlike structure due to the accumulation of active particles in regions of high curvature and rigidity—a configuration not typically observed in flexible polymers [28,30,71].

In Figs. 12(a) and 12(b), we plot the probability density function for $R_{A_i-A_j}$ for flexible ($\kappa = 0$) and semiflexible ($\kappa = 75$) star polymers. As shown in Fig. 12(a), for the flexible polymer in the range $Pe = 0, \dots, 20$, there is no emergence of a peak at lower values of $R_{A_i-A_j}$; instead, the distribution broadens with increasing values of Pe . In contrast, for the semiflexible polymer case shown in Fig. 12(b), at $Pe = 0$, the distribution is peaked at a higher value of $R_{A_i-A_j}$. On increasing the activity to $Pe = 10$, a new peak emerges at a lower value of $R_{A_i-A_j}$, and its intensity increases further at $Pe = 20$, accompanied by a broader distribution at larger values of $R_{A_i-A_j}$. A similar distribution of conformations is also observed for flexible polymers at $Pe = 50$ in Fig. 2, further supporting the observation that higher bath activity reduces the effects of polymer stiffness. As discussed previously, the shown distribution corresponds to conformations in which two arms of the polymer are paired, while the third arm is located at a certain distance. Based on these observations, we conclude that the interplay between polymer rigidity and interactions with active particles favors such conformations even at low Pe in the case of semiflexible polymers.

In addition to calculating the inter-arm distance $R_{A_i-A_j}$ and the arm-arm angle $\theta_{A_i-A_j}$, we compute the gyration tensor for the star polymers, defined as

$$S = \frac{1}{N_{\text{beads}}} \begin{pmatrix} \sum_i (x_i - x_{\text{com}})^2 - \lambda_1^2 & \sum_i (x_i - x_{\text{com}})(y_i - y_{\text{com}}) \\ \sum_i (x_i - x_{\text{com}})(y_i - y_{\text{com}}) & \sum_i (y_i - y_{\text{com}})^2 - \lambda_2^2 \end{pmatrix}, \quad (8)$$

where x_{com} and y_{com} denote the coordinates of the polymer’s center of mass, and $N_{\text{beads}} = 61$ is the total number of beads in the star polymer. To analyze the shape anisotropy, we diagonalize the gyration tensor (8) to obtain its principal components

$$S = \text{diag}(\lambda_1^2, \lambda_2^2), \quad (9)$$

where λ_1^2 and λ_2^2 are the eigenvalues of the tensor. The first invariant of S yields the squared radius of gyration

$$R_g^2 = \text{Tr}(S) = \lambda_1^2 + \lambda_2^2. \quad (10)$$

We compute the time and ensemble-averaged value of R_g^2 as a function of the Péclet number Pe across multiple trajectories. Specifically, in Fig. 12(c), we plot the averaged squared radius of gyration ($\langle R_g^2(Pe) \rangle$) as a function of the bath activity for both flexible (black) and semiflexible (red) star polymers. At vanishing activity ($Pe = 0$), the flexible star polymer has compact, coiled conformations, resulting in smaller $\langle R_g^2 \rangle$ values. As the activity increases, collisions with active particles lead to a swelling of the polymer, reflected in increased $\langle R_g^2 \rangle$ values.

In contrast, the semiflexible star polymer adopts an extended conformation at $Pe = 0$, primarily due to the effect of arm rigidity. As activity increases, $\langle R_g^2 \rangle$ decreases, which we attribute to the pairing and bending of arms caused by the asymmetric accumulation of active particles in regions of high curvature of the polymer. An intriguing feature emerges at high activity levels: The effect of activity starts to dominate over the rigidity of the arms, as mentioned above. As a result, the values of $\langle R_g^2 \rangle$ for both flexible and semiflexible star polymers begin to converge, indicating that both types of polymers adopt similar conformations under strong activity. This swelling and collapsing behavior of the flexible and semiflexible star polymers in an active bath is similar to that observed for flexible and semiflexible linear polymers, respectively [28,71].

2. Dynamics of the star polymer

In the existing literature, it has been explored how the activity of bath particles facilitates a prolonged persistent motion of asymmetric hard passive particles [35–37]. The persistent motion of an object in a given direction in some

sense closely mirrors what Feynman described in his well-known “Ratchet-and-Paw” lecture, in which he explored the second law of thermodynamics through the lens of statistical mechanics. The idea of harnessing work from a chaotic environment through rectification depends on breaking both time-reversal and spatial-inversion symmetries. In Feynman’s example, time-reversal symmetry is disrupted by using two thermal baths at different temperatures, while in another case, it is broken by a bath of active particles with inherently irreversible dynamics [72]. This disruption violates detailed balance, a condition in equilibrium systems where forward and reverse processes occur with equal likelihood. When time-reversal symmetry is no longer valid, breaking spatial symmetry—such as by using an asymmetrically shaped gear or shuttle—can enable rectification and thus allow for directed motion or work extraction [73,74]. Experimentally, energy extraction from a symmetric stochastic process in the sense of a Maxwell demon could indeed be demonstrated for a colloidal particle [75].

It is important to understand such partially rectified dynamics in the context of soft particles with elongated topologies [36]. Recent studies have focused on soft linear polymers in active baths, where the polymers exhibit significantly enhanced dynamics [28,76]. Beyond linear deformable polymers, the behavior of other topologies has also been explored in active environments [77]. In this context, to further advance our understanding of passive polymers in active media, we investigate the dynamics of a three-armed flexible star polymer immersed in a bath of ABPs as a function of time. Due to the presence of the active particles, the star polymer switches between several conformations, as discussed in the previous section. As we show now, this also affects intriguing dynamic behavior.

To quantify these effects, we track the center-of-mass position r_i^{com} of the star polymer and compute the componentwise time-averaged mean-squared displacement (TAMSD) as a function of the lag time τ [78–80]

$$\overline{\delta r_i^2(\tau)} = \frac{1}{T_{\text{max}} - \tau} \int_0^{T_{\text{max}} - \tau} (r_i^{\text{com}}(t + \tau) - r_i^{\text{com}}(t))^2 dt, \quad (11)$$

whose average over a number N of independent trajectories is the ensemble-averaged (mean) TAMSD [78–80]

$$\langle \overline{\delta r_i^2(\tau)} \rangle = \frac{1}{N} \sum_{i=1}^N \overline{\delta r_i^2(\tau)}. \quad (12)$$

For Brownian motion, the mean TAMSD $\langle \overline{\delta r_i^2(\tau)} \rangle$ grows linearly with lag time τ . However, in the presence of ergodic anomalous dynamics, we observe a power-law scaling of the form

$$\langle \overline{\delta r_i^2(\tau)} \rangle \propto \tau^\alpha, \quad (13)$$

where $\alpha < 1$ indicates subdiffusion and $\alpha > 1$ indicates superdiffusion [80–82].

In Fig. 4(a), we plot the time evolution of the mean TAMSD [Eq. (12)] for different values of the Péclet number Pe . It is evident that upon increasing the activity Pe of the active particles leads to an enhancement of the motion as measured by $\langle \overline{\delta r_i^2(\tau)} \rangle$. This enhancement arises from frequent

encounters and asymmetric accumulation of active particles around the polymer. The extent of this enhancement is related to the persistent motion of the polymer, which is evident in Fig. 4(b), where we show how $\alpha(\tau)$ increases with Pe , indicating a pronounced transient superdiffusive behavior and thus enhanced persistence. Further evidence of the prolonged persistent motion is provided by the VACF and the effective persistence time τ_p of the center of mass motion of a passive star polymer [83], as shown in Figs. 4(c) and 4(d), respectively. The VACF is here defined over the time average

$$\text{VACF} = \frac{\langle v_i(t + \tau)v_i(t) \rangle}{\langle v_i^2(t) \rangle}, \quad (14)$$

where v_i is a component of the velocity \mathbf{v}_{com} of the polymer’s center of mass. The effective persistence time (τ_p) is defined as the duration during which the center of mass of the polymer maintains its motion in a given direction. It is mathematically expressed as

$$\tau_p = \int_0^{t^*} \text{VACF} dt, \quad (15)$$

where t^* is the time at which the VACF reaches zero.

In Fig. 4(c), we observe that beyond $Pe = 20$ the VACF exhibits a pronounced positive temporal correlation that extends over a longer period for the higher Pe values $Pe = 30$ and 50 , indicating prolonged persistent motion. To quantify the enhancement in the persistence, we plot the relative persistence time (15) as a function of Pe in Fig. 4(d). For $Pe \leq 20$, there is no significant effect, and the ratio remains nearly constant. However, beyond $Pe \approx 20$, there is a noticeable increase in the persistence time with activity. Notably, the Pe value at which this significant increase in the persistence time occurs coincides with the emergence of a distinct polymer conformation: the pairing of two arms while the third arm remains separated. We conclude that the persistent motion of the star polymer is closely linked to this conformation, which is governed by the asymmetric accumulation of active particles.

Another fundamental quantity of interest for understanding the star polymer dynamics is the intermediate scattering function (ISF), defined as a function of the difference in the center of mass position as separated by the lag time τ ,

$$F_s(k, \tau) = \langle \exp(-ik(r_j^{\text{com}}(\tau) - r_j^{\text{com}}(0))) \rangle, \quad (16)$$

where $r_j^{\text{com}}(\tau)$ and $r_j^{\text{com}}(0)$ are the positions of the center of mass of the polymer at times τ and 0 , respectively. The symbol $\langle \cdot \rangle$ again denotes averaging over different trajectories. In Fig. 5(a), we plot the time evolution of $F_s(k, \tau)$ for $k = 1.0$ at different values of Pe . It is evident that the decay of $F_s(k, \tau)$ becomes faster with increasing Pe as compared to the case $Pe = 0$ in the absence of activity.

In the case of Brownian dynamics, the dependence of the intermediate scattering function (16) on k is given by

$$F_s(k, \tau) = \exp(-Dk^2\tau) = \exp\left(-k^2\left[\frac{\tau}{\tau_s}\right]\right), \quad (17)$$

where in the second equality we used the fact that the diffusivity D is related to the relaxation time τ_s via $\tau_s = 1/D$ [84].

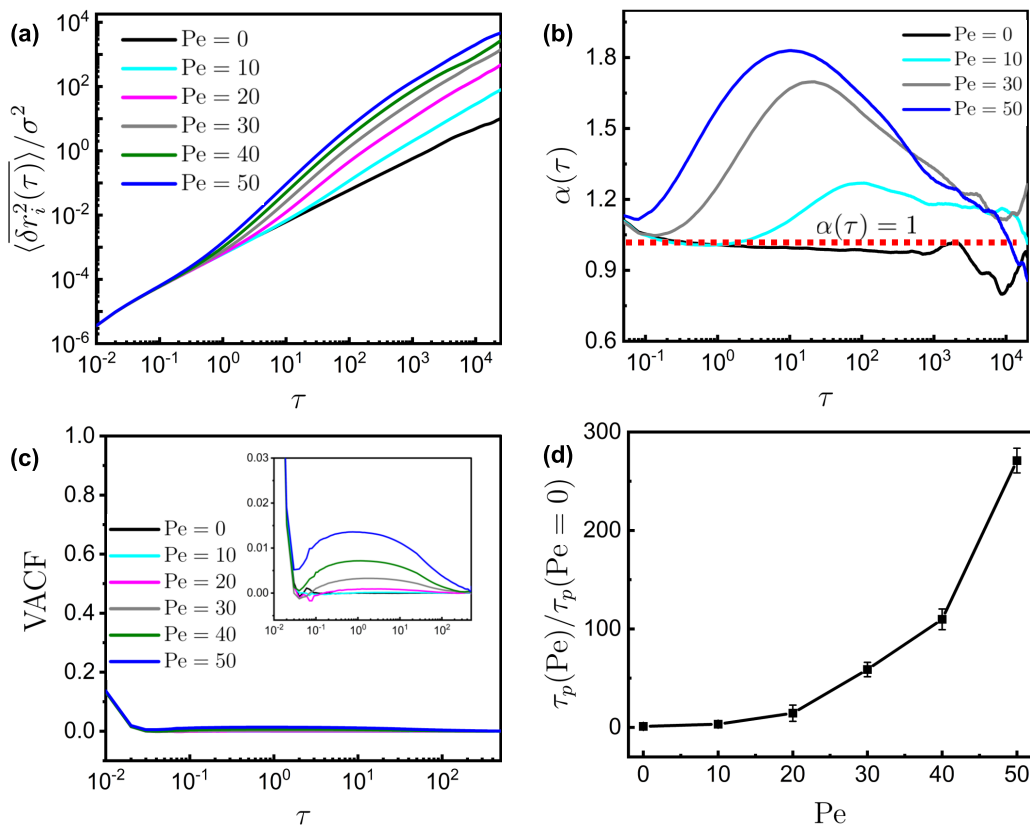


FIG. 4. Log-log plot of the time evolution of (a) the mean TAMSD $\overline{\langle \delta r_i^2(\tau) \rangle}$; log-linear plots of (b) the time-local anomalous diffusion exponent $\alpha(\tau)$, along with the (c) VACF of the motion for different values of Pe and (d) the relative effective persistence time $\tau_p(\text{Pe}) / \tau_p(\text{Pe} = 0)$ at some value of Pe divided by its inactive value, as a function of Pe for the center of mass motion of the star polymer. Inset in panel (c) shows a magnified view of the same.

Since our star polymers in the active bath exhibit pronounced persistent motion—especially at high activity—deviations from the simple exponential form (17) are expected. To account for this, we employ the modified exponential form

$$F_s(k, \tau) = \exp\left(-\left[\frac{\tau}{\tau_s(k)}\right]^\beta\right), \quad (18)$$

where β is the stretching coefficient. For $0 < \beta < 1$ the form (18) is referred to as a “stretched exponential function” [85] or Kohlrausch-Williams-Watts (KWW) form, historically linked to the works of Kohlrausch [86] and Williams and Watts [87]; see also Refs. [88–91]. Values of $\beta > 1$ in relation (18) produce a “compressed exponential” behavior. The exponent β characterizes the extent to which the decay of $F_s(k, \tau)$ is faster than the simple exponential decay, the latter being the

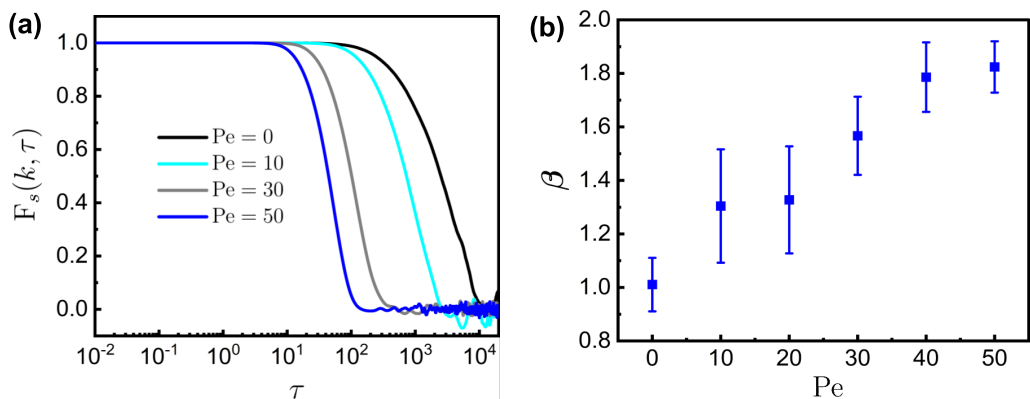


FIG. 5. Log-linear plots showing the time evolution of the intermediate scattering function [Eq. (16)] for (a) wave number $k = 1$. Panel (b) shows the change in the compressed exponential coefficient β defined in Eq. (18) as a function of Pe.

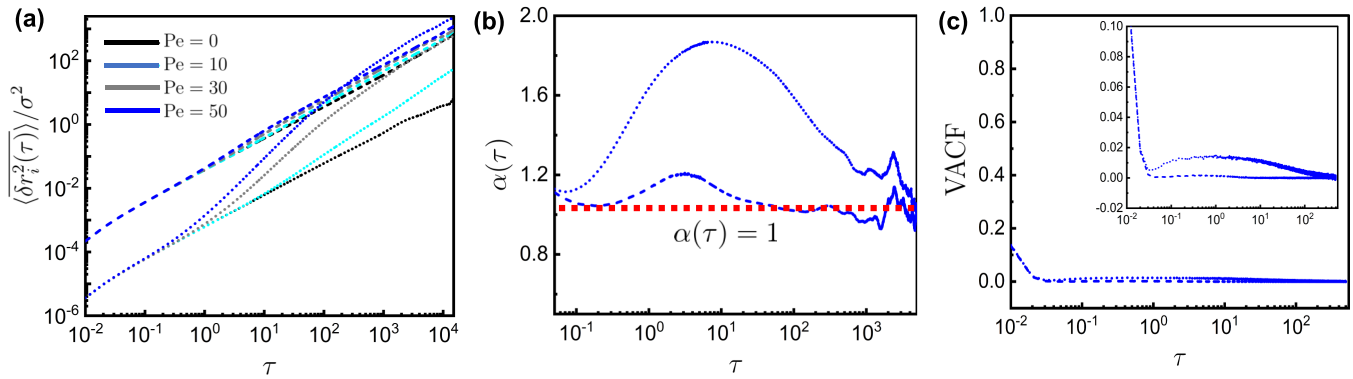


FIG. 6. Time evolution of the (a) mean TAMSD $\overline{\langle \delta^2 r_i^2(\tau) \rangle}$ on log-log scale for different activities Pe , (b) time-local anomalous diffusion exponent $\alpha(\tau)$ on log-linear scale at $Pe = 50$, and (c) VACF on log-linear scale at $Pe = 50$ for the COM of the star polymer (dotted lines) and the single colloidal particle (dashed lines). The inset in panel (c) shows the significant range of positive correlations as compared to the single particle, whose VACF remains approximately zero throughout.

hallmark of Brownian dynamics. In Fig. 5(b), we plot the variation of β with Pe for $k = 1$. At $Pe = 0$, we observe $\beta = 1$, and Eq. (18) reduces to the Brownian form given in Eq. (17). As activity increases, β becomes greater than unity and continues to grow with increasing Pe . A faster relaxation dynamics with $\beta > 1$ is in fact typical in systems exhibiting long persistence times and for sufficiently high Pe , when the dynamics of the star polymer approaches those of free ABPs, we expect β will become independent of the active force; further increases in activity will then primarily affect τ_s and the diffusivity [92,93]. We show that the intermediate scattering function relaxes more rapidly at larger values of k at other activity levels, as well (see Fig. 13).

B. Comparison of the behavior of a passive particle and a star polymer in a dilute active bath

The dynamics of passive colloidal particles and linear polymers in an active bath were shown to enhance the particle diffusion, often affecting (transient) superdiffusion [19–22,22–34]. In particular, it was shown that linear polymers in active baths have intriguing conformational and dynamic properties. To further investigate the effect of the polymer topology, we compare the dynamics of our star polymer with other entities, starting with a single particle. To this end, we simulated a passive particle of diameter σ in a dilute active bath; the results are displayed in Fig. 6, in comparison with the dynamics of our three-armed star polymer. In Fig. 6(a), we show the componentwise mean TAMSDs of the single particle position r_i and of the center-of-mass position r_i^{com} of the star polymer. In the passive case ($Pe = 0$), the dynamics remain normal-diffusive, regardless of the tracer topology, as shown in Fig. 6(a). The differences in the amplitude arise due to the effective tracer size: the colloidal particle exhibits a faster dynamics in comparison to the larger star polymer. With increasing activity, the dynamics of colloidal particles show only a slight change, indicating that activity has no profound effect on their motion. In contrast, the star polymer displays a significant enhancement in the mean TAMSD with increasing activity. This enhancement is also evident from the larger values of the anomalous diffusion exponent

$\alpha(\tau)$ for the case $Pe = 50$ for the star polymer as compared to the passive colloidal particle in Fig. 6(b).

The high values of $\alpha(\tau)$ along with the longer relaxation time toward the normal-diffusive regime with $\alpha = 1$ observed for the star polymer, as compared to the colloidal particle, indicate a more persistent and effective motion in the presence of activity. The prolonged persistent motion of the star polymer with a positive VACF, relative to the passive colloidal particle, as shown in Fig. 6(c) supports the increase of the mean TAMSD for larger Péclet numbers. Note that for the highest Péclet number shown ($Pe = 50$), the mean TAMSD of the star polymer even overshoots the values of the single particle at longer times, despite the larger size of the star polymers. The VACF shown in Fig. 6(c) demonstrates the relatively long time range over which the star polymer has significant positive correlations, before eventually decaying to zero.

C. Comparison of the behavior of a linear polymer with 41 beads and the three-armed star polymer in a dilute active bath

We now compare the dynamics of our star polymer with that of a linear polymer. We choose the size of 41 beads for the linear polymer, as in this case we expect that the behavior of star and linear polymers becomes approximately the same at high activity, when the star polymer has two aligned arms. The mean TAMSD of both polymers is shown in Fig. 7(a) along with the long-time diffusivity

$$D = \lim_{\tau \rightarrow \infty} \frac{1}{4\tau} \overline{\langle \delta r_i^2(\tau) \rangle} \quad (19)$$

in Fig. 7(b). Indeed, at high Pe the effective long-time diffusivity of both topologies converges, despite the fact that the star polymer consists of 61 monomers as compared to the 41 of the linear chain. This difference causes the smaller diffusivity and amplitude of the mean TAMSD at smaller Pe . In Fig. 7(c), we plot the VACF of the center of mass for the linear polymer (solid line) and the star polymer (dotted line) for $Pe = 50$. In this high-activity case, both show very similar behavior with extended-in-time positive correlations. To understand the structural features of the polymers underlying

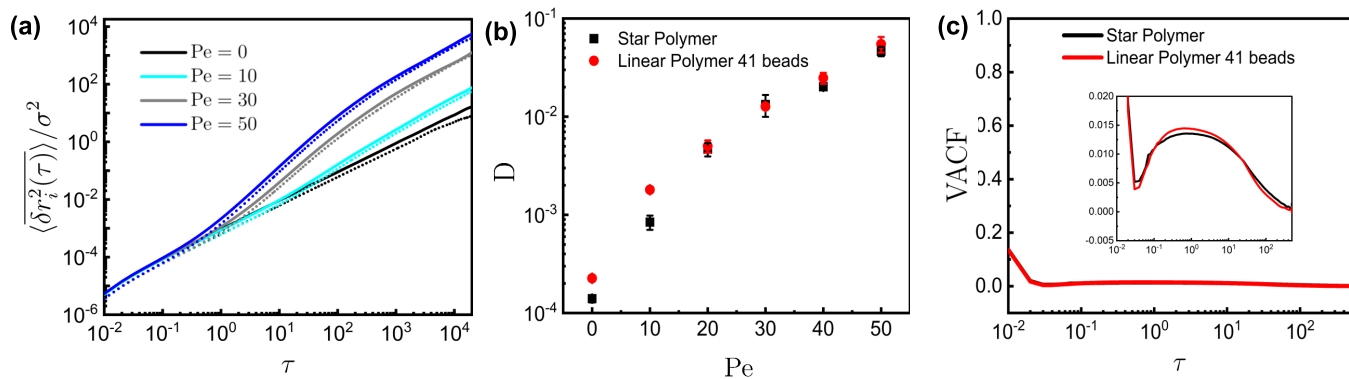


FIG. 7. (a) Log-log plot of the mean TAMSD vs the lag time for the COM of the star polymer (dotted lines) and a linear polymer (41 beads, solid lines). (b) Linear-log plot of the diffusivity of the COM for the star polymer (black) and the linear polymer (red) as a function of Pe . (c) VACF on a log-linear scale at $Pe = 50$ for the COM of the star polymer (61 beads, black) and the linear polymer (41 beads, red). The inset in panel (c) shows a magnified view with a clear local minimum at short times.

the observed convergence of their dynamics at high Pe , we plot the probability density function of the radius of gyration R_g for the star polymer (black line) and the linear polymer (red line) at different values of the Péclet number in Fig. 8. Specifically, in absence of activity ($Pe = 0$) in Fig. 8(a), the density for the star polymer is peaked at a higher value of R_g compared to that of the linear polymer. Additionally, the distribution for the linear polymer is more broadly spread. Upon increasing the activity to $Pe = 20$, the difference between the distributions diminishes, and at high activity with $Pe = 40$ in Fig. 8(c), the distributions cover almost the same range of R_g . The convergence in the distributions for the linear and star polymers at high activity confirms the similarity in their structural features. This also supports the pairing of two arms of the star polymer, while the third arm remains at a variable distance, resulting in a conformation similar to that of a linear polymer in an active bath, due to the effective pressure exerted by the accumulating ABPs in regions of higher curvature. In both cases, the accumulation of ABPs increases with increasing activity, as demonstrated in Fig. 14. The similarity in the structure of linear and star polymers at high Pe is also evident in Fig. 15(a), where the difference in the squared radius of gyration between the star and linear polymers decreases with increasing Pe and nearly vanishes at high Pe .

D. Comparison of the behavior of a linear polymer with 61 beads and a three-armed star polymer in a dilute active bath

In Fig. 9, we compare the radius of gyration of a three-armed star polymer and a linear polymer for the case when both have the same total number of monomers. In Fig. 9(a), we plot the probability density function of the radius of gyration for the three-armed star polymer (black) and the linear polymer (red) at $Pe = 0$. The distribution is peaked at a higher value for the linear polymer as compared to the star polymer, reflecting the effect of topology on the polymer extension. As the activity increases to $Pe = 20$, as shown in Fig. 9(b), and then to $Pe = 40$ shown in Fig. 9(c), the difference between the two topologies becomes more pronounced; specifically, the distribution for the linear polymer broadens and shifts further to higher values of R_g . This difference in extension is also evident in Fig. 15(b), where we plot the difference in the average squared radius of gyration between the linear and star polymers as a function of activity. The difference indeed increases monotonically with Pe , supporting the intuition that the pairing of arms in the star polymer, along with its more complex topology, limits its extension under active conditions.

To analyze further the effect of topology on the polymer dynamics, we plot the time evolution of the mean TAMSD of

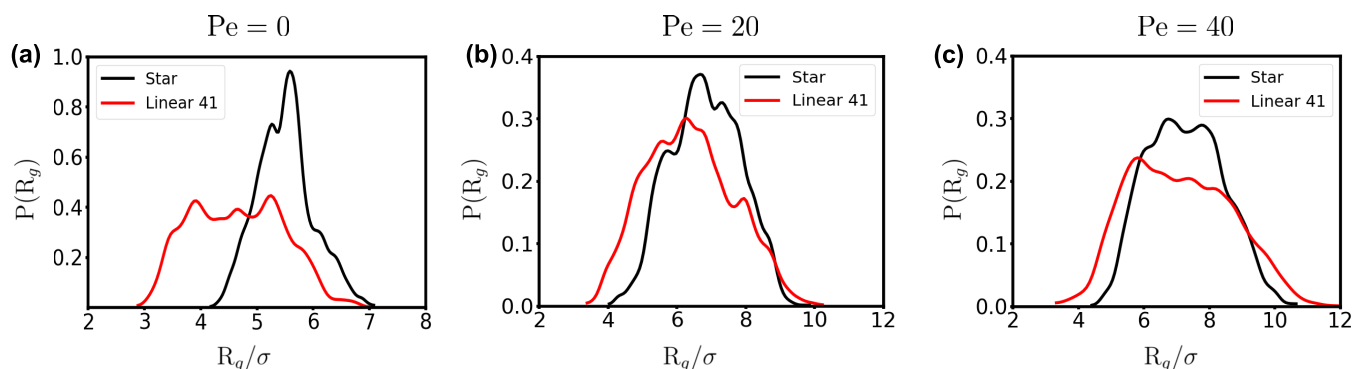


FIG. 8. Probability density function of the gyration radius for the star polymer (61 beads, black) and the linear polymer (41 beads, red) for (a) $Pe = 0$, (b) $Pe = 20$, and (c) $Pe = 40$.

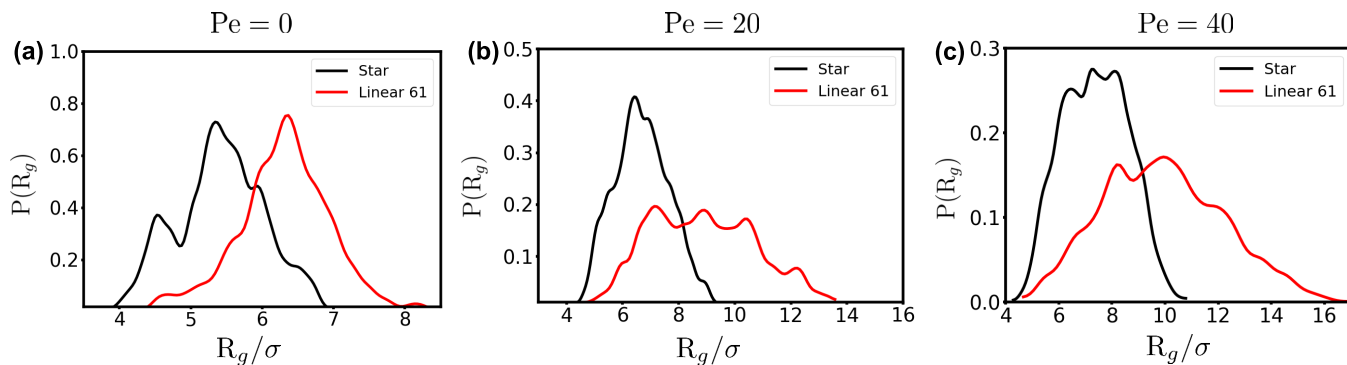


FIG. 9. Probability density function of the gyration radius for the star polymer (black line) and the linear polymer (61 beads, red line) at (a) $Pe = 0$, (b) $Pe = 20$, and (c) $Pe = 40$.

the center of mass and the corresponding long-time diffusivity in Fig. 10. Figure 10(a) demonstrates that at lower activity levels ($Pe \leq 20$), the mean TAMSD of the center of mass for both the linear polymer (61 beads) and the star polymer with three arms (also 61 beads) are nearly identical. However, at higher activity, specifically at $Pe = 50$, the mean TAMSD of the star polymer exceeds that of the linear polymer. This supports the observation related to the structural features of the polymers: While the linear polymer extends more readily, the arms of the star polymer tend to pair, limiting its extension. A similar trend is observed in Fig. 10(b), where the diffusivity of the star polymer is shown to increase significantly at high Pe as compared to that of the linear polymer. This enhancement in the dynamics of the star polymer relative to the linear polymer at high activity is further supported by the time evolution of the VACF, shown in Fig. 10(c). Namely, the VACF for the star polymer (black color) is more positive than that of the linear polymer (red color), confirming the more persistent motion of the star polymer in this high activity regime.

To better understand the effect of topology on transport in a dilute active bath of tracers, we analyze the behavior of tracers with different topologies that vary in the number of arms, N_{arm} , ranging from a single colloidal particle ($N_{\text{arm}} = 0$) to a linear polymer, in which two arms of 20 beads are connected to a central bead, and further to star polymers with $N_{\text{arm}} = 3$ and $N_{\text{arm}} = 4$. We then compare their center-of-mass MSD

$\langle \delta r_i^2(\tau) \rangle$ at $Pe = 50$. As shown in Fig. 16(a), with increasing N_{arm} —from $N_{\text{arm}} = 0$ (colloidal particle) to $N_{\text{arm}} = 2$ (linear polymer)—the dynamics is enhanced, particularly at long times. A further increase to $N_{\text{arm}} = 3$ (a star polymer with three arms) still results in faster center-of-mass dynamics as compared to the colloidal particle and exhibits a behavior similar to that of a linear polymer. This is attributed to the adoption of specific conformations and the asymmetric accumulation of ABPs, as discussed in previous sections. When N_{arm} is increased to four (a star polymer with four arms), $\langle \delta r_i^2(\tau) \rangle$ remains larger than for the colloidal particle but becomes slightly smaller than that of the linear polymer and the three-armed star polymer. The snapshots in Fig. 16(b) indicate that this behavior arises from arm pairing and the accumulation of ABPs around the tracer. From these observations, we conclude that the change in dynamics with increasing number of arms is nonmonotonic. In addition to varying the number of arms, we also simulate a ring polymer consisting of 41 beads in the same active bath. Interestingly, it adopts a quasilinear conformation due to the accumulation of ABPs, as evident from the snapshots in Fig. 16(c). Overall, we find that deformable filaments with the discussed topologies exhibit more efficient transport than single colloidal particles in an active bath. Such enhanced transport, combined with the tunable properties [44–48] of these systems—such as rigidity, chain length, and the number of arms in the star polymer—makes

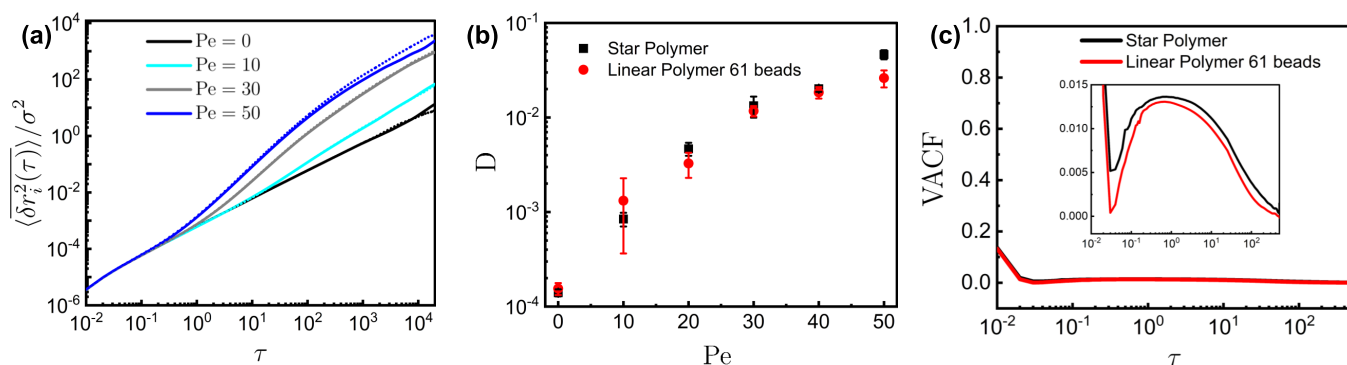


FIG. 10. (a) Log-log plot of the mean TAMSD vs lag time for the COM motion of the linear polymer (61 beads, solid lines) and the star polymer (dotted lines). (b) Linear-log plot of the diffusivity of the COM for the star polymer (black) and the linear polymer (red) as a function of Pe . (c) VACF on a log-linear scale at $Pe = 50$ for the COM motion of the star polymer (black) and the linear polymer (red). The inset in panel (c) shows a magnified view.

them promising candidates for drug-delivery applications. A more detailed study of these parameters would be both intriguing and important for biomedical purposes.

IV. CONCLUSION

We presented an investigation of the dynamics and conformational changes of star polymers in a dilute bath of ABPs using two-dimensional molecular dynamics simulations, and compared their behavior with tracers of other topologies. Our results reveal distinctive conformational responses of star polymers in the active bath. Notably, beyond a certain threshold of activity as measured by the Péclet number Pe , the star polymer adopts a configuration in which two arms pair while the third remains extended—an arrangement driven by the asymmetric accumulation of active particles in regions of higher chain curvature. The pairing of the arms of the star polymer in the active bath resembles observations from previous studies, in which passive tracers (both linear and colloidal) experience depletion-induced attractive forces due to the accumulation of active particles [50–52]. This asymmetry, combined with the arm pairing of the flexible star polymers, results in prolonged directed motion, as evidenced by the enhanced mean TAMSD, sustained positive VACF, and an increased persistence time with increasing Pe .

Semiflexible star polymers exhibit this arm-pairing conformation at lower activity levels as compared to their flexible counterparts, suggesting that polymer rigidity promotes such structural asymmetry. When compared to passive colloidal particles—each having the same size as a single polymer bead—the star polymer exhibits faster and more persistent center-of-mass dynamics at high activity, owing to the same mechanisms of arm pairing and active particle accumulation. This difference is clearly reflected in the higher mean TAMSD larger time-local anomalous diffusion exponents, and more pronounced positive VACF observed for the star polymer as compared to the colloidal particles at high Pe . The persistent dynamics of the star polymer arise from its asymmetric structure and the accumulation of active particles in regions of high curvature [28,36,94].

Interestingly, at high activity, the conformation of the star polymer—with two arms paired and one extended—closely resembles that of a linear polymer. This structural similarity is reflected in their dynamics as well. To explore this, we compared the dynamics of a three-armed star polymer (61 beads) with those of a linear polymer consisting of 41 beads. The results show that their dynamics indeed converge at high Pe .

Furthermore, when comparing a star and a linear polymer with the same number of beads, the star polymer still demonstrates faster and more persistent dynamics at high activity. This distinction is attributed to their conformational differences, as indicated by the smaller radius of gyration of the star polymer relative to the linear chain. Additionally, the velocity autocorrelation function confirms that the star polymer retains a higher level of temporal correlation than the linear polymer under similar conditions. We primarily investigate systems at a packing fraction of $\phi = 0.06$, but previous studies indicate that this effect is valid within the

range of packing fractions where the accumulation of active particles is not sufficient to trap the tracer dynamics [35–38]. In particular, Ref. [38] reports that at packing fractions of $\phi = 0.4$ and $\phi = 0.6$, the polymer experiences trapping due to the stable clustering of active particles in its vicinity. This occurs because, at these packing fractions, active particles undergo phase separation into dense and dilute regions, a phenomenon known as motility-induced phase separation. Although the focus of [38] is on the role of star polymers as nucleation centers for phase separation at $\phi = 0.4$, the dynamics and conformational changes of star polymers were also studied at $\phi = 0.6$, where trapping and subdiffusive behavior are observed. Moreover, the nature of interactions between particle pairs at high packing fractions changes from attractive to repulsive [51]. Our additional simulations at $\phi = 0.15$ and $Pe = 50$ [Fig. 16 (right)] show conformations similar to those at $\phi = 0.06$, suggesting that $\phi = 0.06$ is not the optimal packing fraction for persistent motion. This is because the similar polymer structure and the greater accumulation of active particles at relatively higher packing fractions are expected to promote more persistent motion. A systematic investigation of these parameters would indeed be necessary to determine the exact optimum packing fraction for persistent motion in the future. Overall, we find that deformable filaments with the examined topologies exhibit more efficient transport than single colloidal particles in an active bath. This enhanced transport, together with the tunable characteristics of such systems—such as rigidity, chain length, and the number of arms in star polymers [44–48]—highlights their potential as promising candidates for drug-delivery applications. This comprehensive investigation of these parameters would be both valuable and relevant for biomedical research.

ACKNOWLEDGMENTS

R.S.Y. thanks IIT Bombay for the fellowship. R.C. acknowledges IRCC-IIT Bombay (Project No. RD/0518-IRCCAW0-001) for funding. We acknowledge the SpaceTime-2 supercomputing facility at IIT Bombay for the computing time. R.M. acknowledges the computer facility at the University of Potsdam, Germany, and the German Science Foundation (DFG, Grants No. ME 1535/16-1 and No. ME 1535/22-1).

DATA AVAILABILITY

The data that support the findings of this article are openly available [95].

APPENDIX A: CALCULATION OF THE EFFECTIVE ENERGY BETWEEN ARMS PAIR OF STAR POLYMER

To obtain the effective interaction energy between a pair of arms of the star polymer placed in a dilute active bath at a given center-of-mass separation $R_{A_i-A_j}$, we enforce a specific separation by applying a harmonic bias potential between the polymer arms shown in blue. The star polymer is immersed in an active bath, as schematically illustrated in Fig. 11, where the polymer beads are shown in blue and the active particles

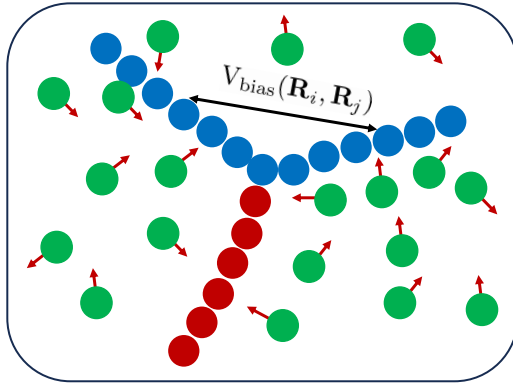


FIG. 11. Schematic depiction of the model system (not to scale): a single star polymer with three arms immersed in an active bath. This system is simulated separately under the influence of a harmonic bias potential, $V_{\text{bias}}(\mathbf{R}_i, \mathbf{R}_j)$, applied between pairs of arms (shown in blue), and immersed in a dilute bath of ABPs (shown in green). The red arrows indicate the instantaneous directions of the ABPs.

in green. The harmonic bias potential used to maintain the specified arm separation is given by [50,51,96]

$$V_{\text{bias}}(\mathbf{R}_i, \mathbf{R}_j) = \frac{1}{2}k'(|\mathbf{R}_i - \mathbf{R}_j| - R_0)^2, \quad (\text{A1})$$

where \mathbf{R}_i and \mathbf{R}_j are the center-of-mass position vectors of the two polymers, k' is the harmonic force constant, R_0 is the equilibrium (or target) separation, and $R_{A_i-A_j} = |\mathbf{R}_i - \mathbf{R}_j|$ is the Euclidean distance between the centers of mass. Each monomer in a chain, located at position \mathbf{r}_i , experiences a confining force given by

$$\mathbf{f}_i = -\left(\frac{\partial V_{\text{bias}}}{\partial R_0}\right) \frac{\partial R_0}{\partial \mathbf{r}_i}. \quad (\text{A2})$$

We start with a separation $R_{A_i-A_j} = 9.0$, which corresponds to the distance between the selected pair of arms at $\text{Pe} = 0$. The star polymer is then simulated in an active bath for the specified value of $R_{A_i-A_j}$ under the influence of the bias

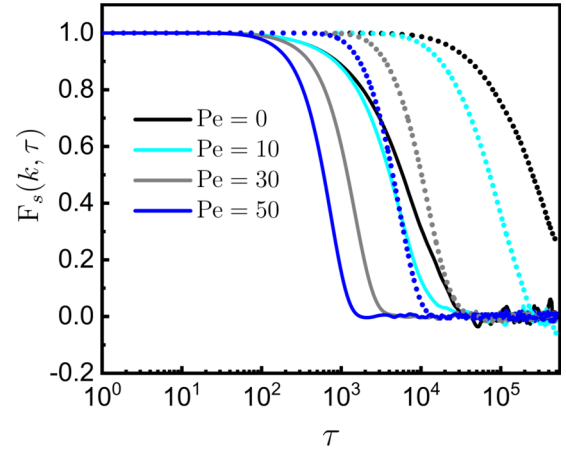


FIG. 13. Log-linear plot showing the time evolution of the self-intermediate scattering function, $F_s(k, \tau)$, for different values of Pe at $k = 1.0$ (dotted lines) and $k = 6.5$ (solid lines).

potential until the system reaches a steady state. To obtain the steady-state conformations, we run biased simulations for 5×10^7 steps and consider the last 3×10^7 steps as steady-state conformations, during which the separation between the centers of mass of the polymer arms remains constant.

Using the steady-state configurations, we calculate the effective force $F^S(R_{A_i-A_j})$ between two arms of the star polymer at a center-of-mass separation $R_{A_i-A_j}$. Since the calculated force $F^S(R_{A_i-A_j})$ includes contributions from the bias potential, the actual force arising from the accumulation of active particles is obtained by subtracting the bias force from the measured $F^S(R_{A_i-A_j})$. The corresponding potential is then calculated by integrating the net force $F^{\text{Snet}}(R_{A_i-A_j})$ over the separation distance,

$$U_{\text{dep}}(R_{A_i-A_j}) = -\int F^{\text{Snet}}(R_{A_i-A_j}) dr,$$

as described in Ref. [97]. We perform 10 independent trajectories, and for each trajectory, there are 3×10^7 steady-state conformations. Thus, the calculated force is effectively averaged over 3×10^8 realizations for each separation.

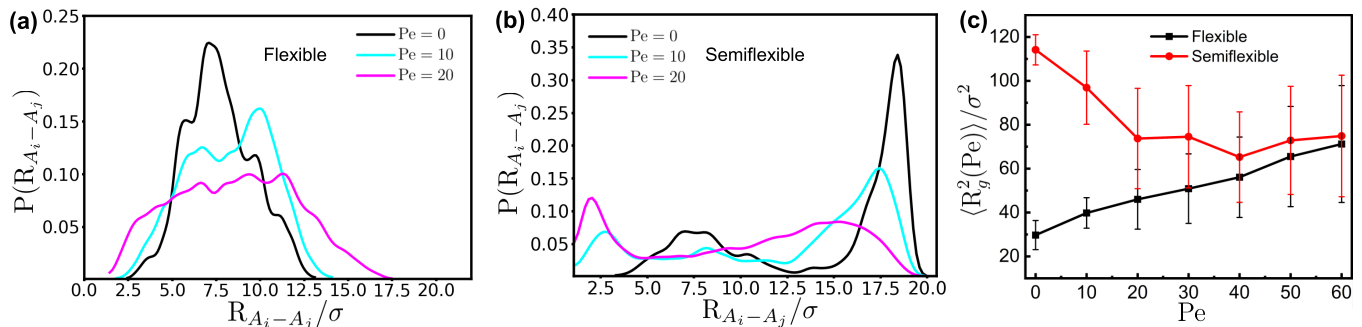


FIG. 12. Probability density function of $R_{A_i-A_j}$ for (a) flexible and (b) semiflexible star polymers. (c) Change in the averaged squared radius of gyration, $\langle R_g^2 \rangle$, as a function of Pe for flexible (black) and semiflexible (red) star polymers.

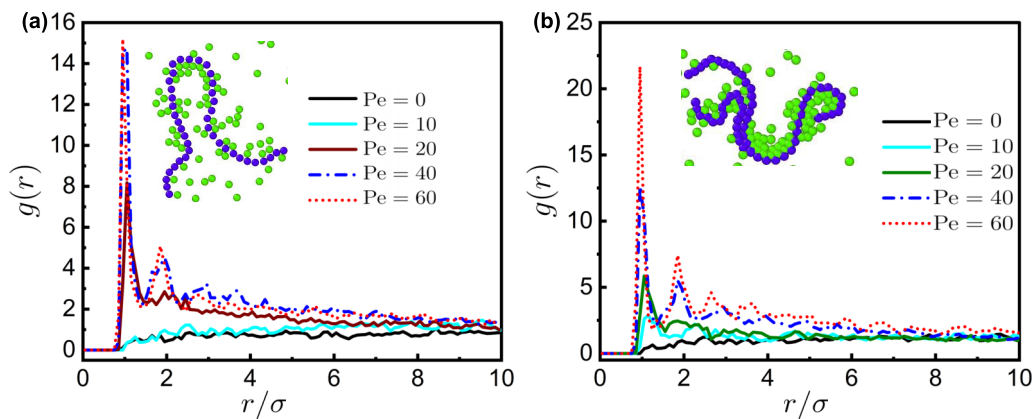


FIG. 14. Radial distribution function of ABPs surrounding (a) a linear polymer and (b) a star polymer. The insets in both panels show snapshots of the respective polymers surrounded by ABPs in an active bath with $Pe = 60$.

APPENDIX B: COMPARISON OF THE STRUCTURAL FEATURES OF FLEXIBLE AND SEMIFLEXIBLE STAR POLYMERS IN AN ACTIVE BATH

To understand the effect of polymer rigidity on the structural features of the star polymer, we plot the probability density function of the arm-arm separation $R_{A_i-A_j}$ for the flexible star polymer in Fig. 12(a) and the semiflexible star polymer in Fig. 12(b). Additionally, we plot the average squared radius of gyration as a function of Pe in Fig. 12(c). The black line corresponds to the flexible polymer ($\kappa = 0$), and the red line depicts the semiflexible polymer ($\kappa = 75$).

APPENDIX C: INTERMEDIATE SCATTERING FUNCTION OF THE CENTER OF MASS MOTION OF THE STAR POLYMER FOR DIFFERENT WAVE NUMBERS IN A DILUTE ACTIVE BATH

For Brownian dynamics, the ISF is given by $F_s(k, \tau) = \exp(-k^2 D \tau)$; i.e., the ISF relaxes faster at higher k values. To understand the dynamics of the center-of-mass motion of a passive star polymer under the influence of the active bath, we plot $F_s(k, \tau)$ at $k = 1.0$ (dotted lines) and $k = 6.5$ (solid lines) in Fig. 13 for different values of Pe . We

observe that, for a given Pe , the ISF relaxes faster at $k = 6.5$ as compared to $k = 1.0$.

APPENDIX D: RADIAL DISTRIBUTION FUNCTION OF ACTIVE BROWNIAN PARTICLES SURROUNDING LINEAR AND STAR POLYMERS

In the case of a linear polymer, prolonged persistent motion is related to the looping of the polymer (“parachute shape”) caused by the accumulation of active particles [28]. To understand the effect of the accumulation of active particles near our star polymer and how this differs from linear polymers, we calculated the radial distribution function $g(r)$, of the ABPs surrounding the polymer filaments, as shown in Fig. 14. We observe that in both cases—linear polymer in Fig. 14(a) and star polymer Fig. 14(b)—there is a noticeable accumulation of ABPs around the polymer. This accumulation becomes more pronounced at higher activity, reflected by an increase in the peak height of $g(r)$ at $r = 1$ with increasing Pe . Furthermore, we observe that with increasing activity, a secondary peak emerges at larger distances. This secondary peak is more pronounced for the star polymer as compared to the linear polymer. From the snapshots shown as insets in the two panels of Fig. 14, we observe that ABP accumulation occurs primarily in regions of higher curvature, which favors

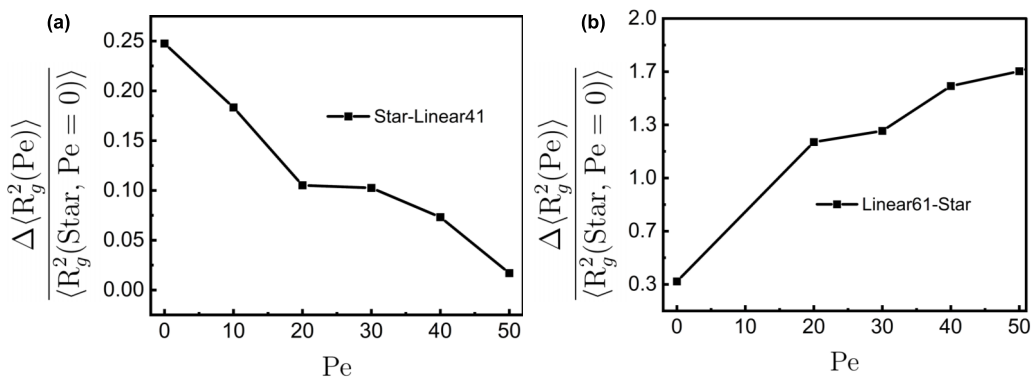


FIG. 15. Relative difference of the average squared radius of gyration as a function Pe for (a) the star polymer and a linear polymer with 41 beads, and (b) the star polymer and a linear polymer with 61 beads.

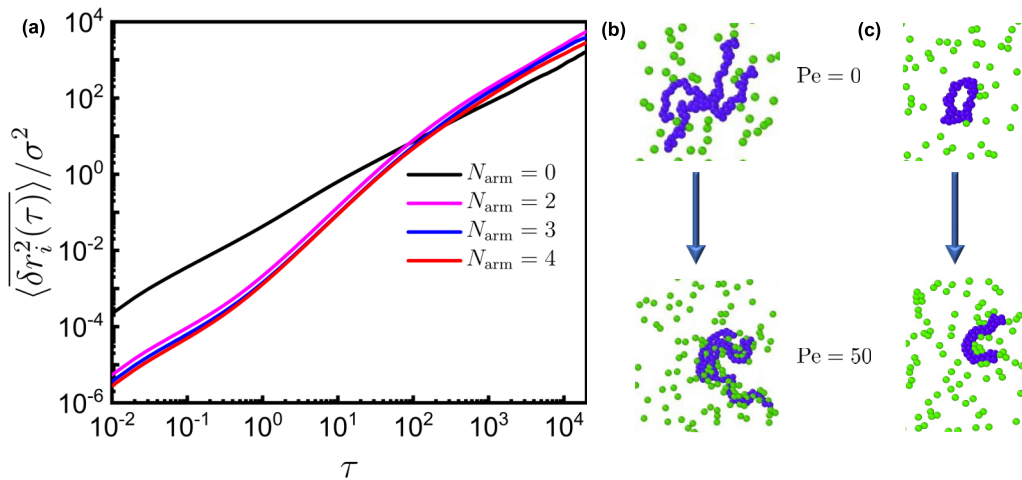


FIG. 16. (a) Log-log plot of the time evolution of the mean TAMSD $\langle \delta r_i^2(\tau) \rangle / \sigma^2$ for tracers with different N_{arm} ; (b) snapshots of the four-arm star polymer at $Pe = 0$ (top) and $Pe = 50$ (bottom); and (c) snapshots of the ring polymer with 41 beads at $Pe = 0$ (top) and $Pe = 50$ (bottom).

a similar structure for both the linear and star polymer at high Pe .

APPENDIX E: DIFFERENCE IN THE SQUARED RADIUS OF GYRATION OF LINEAR AND STAR POLYMERS AS A FUNCTION OF ACTIVITY

Here, we present a plot showing the relative difference in the average squared radius of gyration $\frac{\Delta \langle R_g^2(Pe) \rangle}{\langle R_g^2(\text{Star}, Pe=0) \rangle}$, for a star polymer and a linear polymer with 41 beads in Fig. 15(a), and for a linear polymer with 61 beads and a star polymer in Fig. 15(b). For the star polymer and the linear polymer with 41 beads, the relative difference decreases with increasing Pe , whereas in the case of the linear polymer with 61 beads and the star polymer, it increases.

APPENDIX F: COMPARISON OF THE DYNAMICS OF THE TRACERS HAVING DIFFERENT NUMBERS OF ARMS

Here, we present a plot showing the MSD $\langle \delta r_i^2(\tau) \rangle$ of the center-of-mass of tracers with different numbers of arms, ranging from single colloidal particles ($N_{\text{arm}} = 0$) to a star polymer with four arms ($N_{\text{arm}} = 4$), for $Pe = 50$. The behavior

changes nonmonotonically with increasing number of arms, particularly at long times, as shown in Figs. 16(a) and 16(b) shows snapshots of the four-arm star polymer at $Pe = 0$ (top), where the polymer adopts a coil conformation, and at $Pe = 50$ (bottom), where the polymer folds and pairing of arms becomes evident. Similarly, Fig. 16(c) presents snapshots of a ring polymer consisting of 41 beads at $Pe = 0$ (top), where the ring adopts a coil conformation, and at $Pe = 50$ (bottom), where the ring polymer exhibits a conformation similar to that of a linear polymer due to the accumulation of ABPs.

APPENDIX G: CONFORMATIONS OF THREE-ARMED STAR POLYMER AT PACKING FRACTION $\phi = 0.15$

Three-armed star polymers adopt a coil conformation at $Pe = 0$ and $\phi = 0.15$, as shown in Fig. 17 (left). At $Pe = 50$, they adopt a folded conformation in which two arms of the star polymer are paired, as shown in Fig. 17 (right). The conformations adopted by the three-armed star polymer at the given Pe values are similar to those observed at $\phi = 0.06$, as discussed in the previous sections.

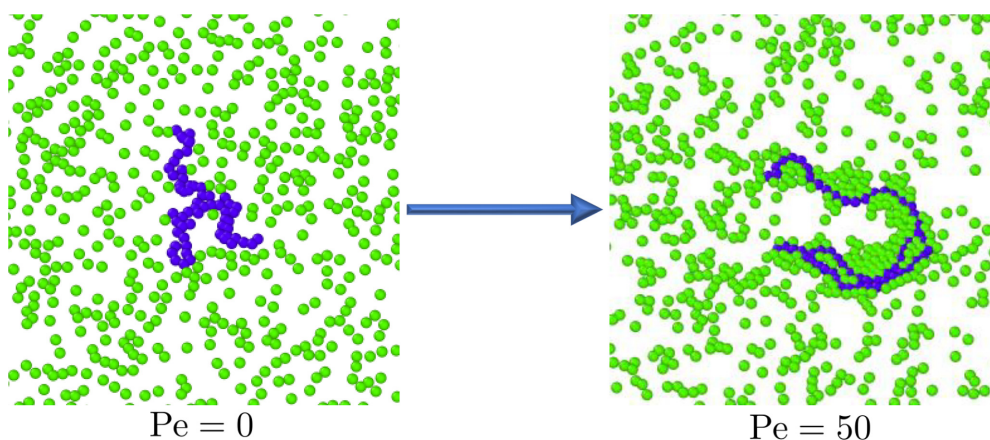


FIG. 17. Snapshots of the three-armed star polymer at $\phi = 0.15$ for $Pe = 0$ (left) and $Pe = 50$ (right).

APPENDIX H: DESCRIPTION OF THE MOVIES

Movie_S1: The movie demonstrates that the passive star polymer (blue) adopts a coil conformation in a bath of ABPs (red) with $Pe = 0$ and $\phi = 0.06$.

Movie_S2: The movie shows that the passive star polymer (blue), in a bath of ABPs (red) with $Pe = 30$ and $\phi = 0.06$,

adopts a swollen conformation. Additionally, we observe an accumulation of ABPs between the arms, facilitating their separation.

Movie_S3: The movie shows that the passive star polymer (blue), in a bath of ABPs (red) with $Pe = 50$ and $\phi = 0.06$, adopts an interesting conformation where two of its arms are paired while the third remains at a distance.

-
- [1] S. Ramaswamy, The mechanics and statistics of active matter, *Annu. Rev. Condens. Matter Phys.* **1**, 323 (2010).
- [2] C. Bechinger, R. Di Leonardo, H. Löwen, C. Reichhardt, G. Volpe, and G. Volpe, Active particles in complex and crowded environments, *Rev. Mod. Phys.* **88**, 045006 (2016).
- [3] W. Wang, W. Duan, S. Ahmed, T. E. Mallouk, and A. Sen, Small power: Autonomous nano-and micromotors propelled by self-generated gradients, *Nano Today* **8**, 531 (2013).
- [4] S. A. Mallory, C. Valeriani, and A. Cacciuto, An active approach to colloidal self-assembly, *Annu. Rev. Phys. Chem.* **69**, 59 (2018).
- [5] S. H. Klapp, Collective dynamics of dipolar and multipolar colloids: From passive to active systems, *Curr. Opin. Colloid Interface Sci.* **21**, 76 (2016).
- [6] M. C. Marchetti, Y. Fily, S. Henkes, A. Patch, and D. Yllanes, Minimal model of active colloids highlights the role of mechanical interactions in controlling the emergent behavior of active matter, *Curr. Opin. Colloid Interface Sci.* **21**, 34 (2016).
- [7] A. M. Menzel, Tuned, driven, and active soft matter, *Phys. Rep.* **554**, 1 (2015).
- [8] J. Bialké, T. Speck, and H. Löwen, Active colloidal suspensions: Clustering and phase behavior, *J. Non-Cryst. Solids* **407**, 367 (2015).
- [9] A. Zöttl and H. Stark, Emergent behavior in active colloids, *J. Phys.: Condens. Matter* **28**, 253001 (2016).
- [10] R. Di Leonardo, Controlled collective motions, *Nat. Mater.* **15**, 1057 (2016).
- [11] G. Frangipane, D. Dell’Arciprete, S. Petracchini, C. Maggi, F. Saglimbeni, S. Bianchi, G. Vizsnyiczai, M. L. Bernardini, and R. Di Leonardo, Dynamic density shaping of photokinetic *E. coli*, *eLife* **7**, e36608 (2018).
- [12] H. Kurtuldu, J. S. Guasto, K. A. Johnson, and J. P. Gollub, Enhancement of biomixing by swimming algal cells in two-dimensional films, *Proc. Natl. Acad. Sci. USA* **108**, 10391 (2011).
- [13] R. Stocker and J. R. Seymour, Ecology and physics of bacterial chemotaxis in the ocean, *Microbiol. Mol. Biol. Rev.* **76**, 792 (2012).
- [14] A. Caspi, R. Granek, and M. Elbaum, Enhanced diffusion in active intracellular transport, *Phys. Rev. Lett.* **85**, 5655 (2000).
- [15] M. Guo, A. J. Ehrlicher, M. H. Jensen, M. Renz, J. R. Moore, R. D. Goldman, J. Lippincott-Schwartz, F. C. Mackintosh, and D. A. Weitz, Probing the stochastic, motor-driven properties of the cytoplasm using force spectrum microscopy, *Cell* **158**, 822 (2014).
- [16] R. Majumdar, A. Saha, and R. Marathe, Exactly solvable model of a passive Brownian heat engine and its comparison with active engines, *J. Stat. Mech.* (2022) 073206.
- [17] D. Martin, J. O’Byrne, M. E. Cates, É. Fodor, C. Nardini, J. Tailleur, and F. Van Wijland, Statistical mechanics of active Ornstein-Uhlenbeck particles, *Phys. Rev. E* **103**, 032607 (2021).
- [18] L. Theycherri, S. Chaki, T. Bhattacharjee, and R. Chakrabarti, Active dynamics of linear chains and rings in porous media, *J. Chem. Phys.* **159**, 014902 (2023).
- [19] P. Pietzonka and U. Seifert, Entropy production of active particles and for particles in active baths, *J. Phys. A: Math. Theor.* **51**, 01LT01 (2018).
- [20] S. Chaki and R. Chakrabarti, Entropy production and work fluctuation relations for a single particle in active bath, *Physica A* **511**, 302 (2018).
- [21] S. Chaki and R. Chakrabarti, Effects of active fluctuations on energetics of a colloidal particle: Superdiffusion, dissipation and entropy production, *Physica A* **530**, 121574 (2019).
- [22] S. Chaki and R. Chakrabarti, Enhanced diffusion, swelling, and slow reconfiguration of a single chain in non-Gaussian active bath, *J. Chem. Phys.* **150**, 094902 (2019).
- [23] S. Ye, P. Liu, F. Ye, K. Chen, and M. Yang, Active noise experienced by a passive particle trapped in an active bath, *Soft Matter* **16**, 4655 (2020).
- [24] J. Shea, G. Jung, and F. Schmid, Passive probe particle in an active bath: Can we tell it is out of equilibrium? *Soft Matter* **18**, 6965 (2022).
- [25] K. Goswami and R. Metzler, Trapped tracer in a non-equilibrium bath: Dynamics and energetics, *Soft Matter* **19**, 8802 (2023).
- [26] R. Großmann, L. S. Bort, T. Moldenhawer, M. Stange, S. S. Panah, R. Metzler, and C. Beta, Non-Gaussian displacements in active transport on a carpet of motile cells, *Phys. Rev. Lett.* **132**, 088301 (2024).
- [27] S. K. Anand and S. P. Singh, Conformation and dynamics of a self-avoiding active flexible polymer, *Phys. Rev. E* **101**, 030501(R) (2020).
- [28] J. Shin, A. G. Cherstvy, W. K. Kim, and R. Metzler, Facilitation of polymer looping and giant polymer diffusivity in crowded solutions of active particles, *New J. Phys.* **17**, 113008 (2015).
- [29] A. Kaiser, S. Babel, B. ten Hagen, C. von Ferber, and H. Löwen, How does a flexible chain of active particles swell? *J. Chem. Phys.* **142**, 124905 (2015).
- [30] K. Goswami, S. Chaki, and R. Chakrabarti, Reconfiguration, swelling and tagged monomer dynamics of a single polymer chain in Gaussian and non-Gaussian active baths, *J. Phys. A: Math. Theor.* **55**, 423002 (2022).
- [31] N. Samanta and R. Chakrabarti, Chain reconfiguration in active noise, *J. Phys. A: Math. Theor.* **49**, 195601 (2016).

- [32] M. S. Aporvari, M. Utkur, E. U. Saritas, G. Volpe, and J. Stenhammar, Anisotropic dynamics of a self-assembled colloidal chain in an active bath, *Soft Matter* **16**, 5609 (2020).
- [33] A. Ghosh and N. Gov, Dynamics of active semiflexible polymers, *Biophys. J.* **107**, 1065 (2014).
- [34] D. Osmanović and Y. Rabin, Dynamics of active rouse chains, *Soft Matter* **13**, 963 (2017).
- [35] A. Kaiser, A. Peshkov, A. Sokolov, B. Ten Hagen, H. Löwen, and I. S. Aranson, Transport powered by bacterial turbulence, *Phys. Rev. Lett.* **112**, 158101 (2014).
- [36] L. Angelani and R. Di Leonardo, Geometrically biased random walks in bacteria-driven micro-shuttles, *New J. Phys.* **12**, 113017 (2010).
- [37] F. Smallenburg and H. Löwen, Swim pressure on walls with curves and corners, *Phys. Rev. E* **92**, 032304 (2015).
- [38] R. S. Yadav, S. Sharma, R. Metzler, and R. Chakrabarti, A passive star polymer in a dense active bath: Insights from computer simulations, *Soft Matter* **20**, 3910 (2024).
- [39] R. G. Winkler, J. Elgeti, and G. Gompper, Active polymers—Emergent conformational and dynamical properties: A brief review, *J. Phys. Soc. Jpn.* **86**, 101014 (2017).
- [40] S. Mallory, C. Valeriani, and A. Cacciuto, Curvature-induced activation of a passive tracer in an active bath, *Phys. Rev. E* **90**, 032309 (2014).
- [41] P. Pérot, M. Lecuit, and M. Eloit, Astrovirus diagnostics, *Viruses* **9**, 10 (2017).
- [42] A. de la Cotte, C. Wu, M. Trevisan, A. Repula, and E. Grelet, Rod-like virus-based multiarm colloidal molecules, *ACS Nano* **11**, 10616 (2017).
- [43] A. B. Zavala-Martínez and E. Grelet, M13-phage-based star-shaped particles with internal flexibility, *ACS Nano* **18**, 281 (2024).
- [44] D.-P. Yang, M. N. N. L. Oo, G. R. Deen, Z. Li, and X. J. Loh, Nano-star-shaped polymers for drug delivery applications, *Macromol. Rapid Commun.* **38**, 1700410 (2017).
- [45] A. Sulistio, J. Lowenthal, A. Blencowe, M. N. Bongiovanni, L. Ong, S. L. Gras, X. Zhang, and G. G. Qiao, Folic acid conjugated amino acid-based star polymers for active targeting of cancer cells, *Biomacromolecules* **12**, 3469 (2011).
- [46] J. Liu, H. Duong, M. R. Whittaker, T. P. Davis, and C. Boyer, Synthesis of functional core, star polymers via raft polymerization for drug delivery applications, *Macromol. Rapid Commun.* **33**, 760 (2012).
- [47] S. Biffi, R. Cerbino, F. Bomboi, E. M. Paraboschi, R. Asselta, F. Sciortino, and T. Bellini, Phase behavior and critical activated dynamics of limited-valence DNA nanostars, *Proc. Natl. Acad. Sci. USA* **110**, 15633 (2013).
- [48] D. Liu, S. H. Park, J. H. Reif, and T. H. LaBean, DNA nanotubes self-assembled from triple-crossover tiles as templates for conductive nanowires, *Proc. Natl. Acad. Sci. USA* **101**, 717 (2004).
- [49] T. Taddese, P. Carbone, and D. L. Cheung, Thermodynamics of linear and star polymers at fluid interfaces, *Soft Matter* **11**, 81 (2015).
- [50] M. Gandikota and A. Cacciuto, Effective forces between active polymers, *Phys. Rev. E* **105**, 034503 (2022).
- [51] R. Ni, M. A. Cohen Stuart, and P. G. Bolhuis, Tunable long range forces mediated by self-propelled colloidal hard spheres, *Phys. Rev. Lett.* **114**, 018302 (2015).
- [52] L. Angelani, C. Maggi, M. Bernardini, A. Rizzo, and R. Di Leonardo, Effective interactions between colloidal particles suspended in a bath of swimming cells, *Phys. Rev. Lett.* **107**, 138302 (2011).
- [53] P. Kushwaha, V. Semwal, S. Maity, S. Mishra, and V. Chikkadi, Phase separation of passive particles in active liquids, *Phys. Rev. E* **108**, 034603 (2023).
- [54] C. Tiwari and S. P. Singh, Collective dynamics of active dumbbells near a circular obstacle, *Soft Matter* **20**, 4816 (2024).
- [55] K. Mondal, P. Bera, and P. Ghosh, Diverse morphology and motility induced emergent order in bacterial collectives, *J. Chem. Phys.* **161** (2024).
- [56] S. M. Mousavi, G. Gompper, and R. G. Winkler, Active bath-induced localization and collapse of passive semiflexible polymers, *J. Chem. Phys.* **155**, 044902 (2021).
- [57] J. R. Howse, R. A. Jones, A. J. Ryan, T. Gough, R. Vafabakhsh, and R. Golestanian, Self-motile colloidal particles: From directed propulsion to random walk, *Phys. Rev. Lett.* **99**, 048102 (2007).
- [58] M. Jehser and C. N. Likos, Aggregation shapes of amphiphilic ring polymers: From spherical to toroidal micelles, *Colloid. Polym. Sci.* **298**, 735 (2020).
- [59] J. D. Weeks, D. Chandler, and H. C. Andersen, Role of repulsive forces in determining the equilibrium structure of simple liquids, *J. Chem. Phys.* **54**, 5237 (1971).
- [60] L. Verlet, Computer “experiments” on classical fluids. I. Thermodynamical properties of Lennard-Jones molecules, *Phys. Rev.* **159**, 98 (1967).
- [61] S. Plimpton, Fast parallel algorithms for short-range molecular dynamics, *J. Comput. Phys.* **117**, 1 (1995).
- [62] D. Vlassopoulos and M. Cloitre, Tunable rheology of dense soft deformable colloids, *Curr. Opin. Colloid Interface Sci.* **19**, 561 (2014).
- [63] G. Wei, C. Zhao, J. Hollingsworth, Z. Zhou, F. Jin, Z. Zhang, H. Cheng, and C. C. Han, Mechanism of two-dimensional crystal formation from soft microgel particles, *Soft Matter* **9**, 9924 (2013).
- [64] M. Laurati, J. Stellbrink, R. Lund, L. Willner, D. Richter, and E. Zaccarelli, Starlike micelles with starlike interactions: A quantitative evaluation of structure factors and phase diagram, *Phys. Rev. Lett.* **94**, 195504 (2005).
- [65] S. Gupta, M. Camargo, J. Stellbrink, J. Allgaier, A. Radulescu, P. Lindner, E. Zaccarelli, C. N. Likos, and D. Richter, Dynamic phase diagram of soft nanocolloids, *Nanoscale* **7**, 13924 (2015).
- [66] T. Zhou and J. F. Brady, Active doping controls the mode of failure in dense colloidal gels, *Proc. Natl. Acad. Sci. USA* **121**, e2407424121 (2024).
- [67] M. Ding, X. Duan, and T. Shi, Flow-induced translocation of star polymers through a nanopore, *Soft Matter* **12**, 2851 (2016).
- [68] K. Nagarajan and S. B. Chen, Flow-induced translocation of star polymers through a nanopore, *J. Phys. Chem. B* **123**, 7919 (2019).
- [69] B. M. Erwin, M. Cloitre, M. Gauthier, and D. Vlassopoulos, Dynamics and rheology of colloidal star polymers, *Soft Matter* **6**, 2825 (2010).
- [70] See Supplemental Material at <http://link.aps.org/supplemental/10.1103/qrjy-9yt6> for the three movies Movie_S1, Movie_S2, and Movie_S3 described in Appendix H.

- [71] J. Harder, C. Valeriani, and A. Cacciuto, Activity-induced collapse and reexpansion of rigid polymers, *Phys. Rev. E* **90**, 062312 (2014).
- [72] J. O’Byrne, Y. Kafri, J. Tailleur, and F. van Wijland, Time irreversibility in active matter, from micro to macro, *Nat. Rev. Phys.* **4**, 167 (2022).
- [73] P. Curie, On symmetry in physical phenomena, *J. Phys. (Paris)* **3**, 393 (1894).
- [74] P. Reimann, Brownian motors: Noisy transport far from equilibrium, *Phys. Rep.* **361**, 57 (2002).
- [75] T. Admon, S. Rahav, and Y. Roichman, Experimental realization of an information machine with tunable temporal correlations, *Phys. Rev. Lett.* **121**, 180601 (2018).
- [76] Z. K. Valei and T. N. Shendruk, Scaling laws for passive polymer dynamics in active turbulence, *Phys. Rev. Lett.* **135**, 138301 (2025).
- [77] G. Negro, L. C. Head, L. N. Carenza, T. N. Shendruk, D. Marenduzzo, G. Gonnella, and A. Tiribocchi, Topology controls flow patterns in active double emulsions, *Nat. Commun.* **16**, 1412 (2025).
- [78] Y. He, S. Burov, R. Metzler, and E. Barkai, Random time-scale invariant diffusion and transport coefficients, *Phys. Rev. Lett.* **101**, 058101 (2008).
- [79] E. Barkai, Y. Garini, and R. Metzler, Strange kinetics of single molecules in living cells, *Phys. Today* **65**(8), 29 (2012).
- [80] R. Metzler, J.-H. Jeon, A. G. Cherstvy, and E. Barkai, Anomalous diffusion models and their properties: Non-stationarity, non-ergodicity, and ageing at the centenary of single particle tracking, *Phys. Chem. Chem. Phys.* **16**, 24128 (2014).
- [81] R. Metzler and J. Klafter, The random walk’s guide to anomalous diffusion: A fractional dynamics approach, *Phys. Rep.* **339**, 1 (2000).
- [82] F. Höfling and T. Franosch, Anomalous transport in the crowded world of biological cells, *Rep. Prog. Phys.* **76**, 046602 (2013).
- [83] This persistence time is distinct from the persistence time τ_R of ABPs.
- [84] N. A. Clark, J. H. Lunacek, and G. B. Benedek, A study of Brownian motion using light scattering, *Am. J. Phys.* **38**, 575 (1970).
- [85] T. V. Ramakrishnan and M. Raj Lakshmi, *Non-Debye Relaxation in Condensed Matter* (World Scientific, Singapore, 1987).
- [86] R. Kohlrausch, Theorie des elektrischen rückstandes in der leidener flasche, *Ann. Phys.* **167**, 179 (1854).
- [87] G. Williams and D. C. Watts, Non-symmetrical dielectric relaxation behaviour arising from a simple empirical decay function, *Trans. Faraday Soc.* **66**, 80 (1970).
- [88] M. O. Vlad, R. Metzler, T. F. Nonnenmacher, and M. C. Mackey, Universality classes for asymptotic behavior of relaxation processes in systems with dynamical disorder: Dynamical generalizations of stretched exponential, *J. Math. Phys.* **37**, 2279 (1996).
- [89] D. L. Huber, Statistical model for stretched exponential relaxation in macroscopic systems, *Phys. Rev. B* **31**, 6070 (1985).
- [90] M. F. Shlesinger and E. W. Montroll, On the Williams-Watts function of dielectric relaxation, *Proc. Natl. Acad. Sci. USA* **81**, 1280 (1984).
- [91] R. G. Palmer, D. L. Stein, E. Abrahams, and P. W. Anderson, Models of hierarchically constrained dynamics for glassy relaxation, *Phys. Rev. Lett.* **53**, 958 (1984).
- [92] G. Szamel and E. Flenner, Extremely persistent dense active fluids, *Soft Matter* **20**, 5237 (2024).
- [93] E. Tjhung and L. Berthier, Analogies between growing dense active matter and soft driven glasses, *Phys. Rev. Res.* **2**, 043334 (2020).
- [94] R. Di Leonardo, L. Angelani, D. Dell-Arciprete, G. Ruocco, V. Iebba, S. Schippa, M. P. Conte, F. Mecarini, F. De Angelis, and E. Di Fabrizio, Bacterial ratchet motors, *Proc. Natl. Acad. Sci. USA* **107**, 9541 (2010).
- [95] R. S. Yadav, Data availability statement, GitHub (2025), <https://github.com/RajarshiChakrabarti/Passive-star-polymer-in-active-bath/>.
- [96] K. Kawaguchi, H. Saito, S. Okazaki, and H. Nagao, Molecular dynamics study on the free energy profile for dissociation of ADP from N-terminal domain of Hsp90, *Chem. Phys. Lett.* **588**, 226 (2013).
- [97] J. Chakrabarti, S. Chakrabarti, and H. Löwen, Short ranged attraction and long ranged repulsion between two solute particles in a subcritical liquid solvent, *J. Phys.: Condens. Matter* **18**, L81 (2006).